POLITECNICO
MILANO 1863

SCUOLA DI INGEGNERIA INDUSTRIALE
E DELL'INFORMAZIONE

Consolidation of in-house Satellite Trajectory Generator for Precise Orbit Determination

Tesi di Laurea Magistrale in
Space Engineering - Ingegneria Spaziale

Author: **Giuseppe Enricomaria Esposito**

Student ID: 970081
Advisor: Prof. Francesco Topputo
Co-advisor: Ing. Yannick Enginger
Academic Year: 2021-22

Abstract

Many modern space activities in Low Earth Orbit, including Geodesy, Topography and SAR missions, have seen a drastic increase in the accuracy requirements for the Precise Orbit Determination of their satellites. To answer these needs, new POD softwares are being developed employing Reduced-Dynamic POD algorithms. These blend information coming from GNSS measurements with orbit predictions computed from the spacecraft dynamics to reconstruct past satellite orbits with high precision. However, these programs require precise and flexible input sources for simulations. With this aim, the Precise Orbit Propagator began development.

The aim of this Thesis was to consolidate the state of development of such Propagator by including new force model components and enhancing already existing perturbations via precise environmental modelling. Another included feature concerned the implementation of a discontinuity control process inside the numerical integrators, to limit numeric errors encountered in the presence of orbital control maneuvers.

An assessment study to investigate the impact of all the Force Models on the propagation results was then carried out for several orbit regimes. Results indicated that, to reach sub-meter level in the propagation, all of the included Perturbations need to be employed. A sensitivity analysis of such dynamical models was then conducted, showing that Geopotential and Aerodynamic Drag effects largely vary depending on Gravity Field and Atmospheric Density models, respectively. The dynamical components were then validated against a commercial flight dynamics program. Finally, results showed that the implemented Discontinuity Control process allowed to almost nullify numerical errors introduced by maneuvers.

Having reached the prescribed requirements on numerical accuracy and fidelity of physical models, the next step of the Propagator development is the final validation against real satellite measurements, after which the software will have reached the necessary maturity.

Keywords: Orbit Propagation, Orbit Perturbations, Precise Orbit Determination, Numerical Integration

Abstract in lingua italiana

Molte moderne missioni spaziali in orbita terrestre bassa, come le missioni di Geodesia, Topografia e SAR, sono state interessate da un drastico aumento nei requisiti di accuratezza riguardo la determinazione dell'orbita per i relativi satelliti. Per rispondere a questi requisiti, nuovi software che utilizzano algoritmi di Reduced-Dynamic POD sono in via di sviluppo. Questi programmi combinano misure GNSS con predizioni basate sulla dinamica del satellite per ricostruire, con grande precisione, orbite passate. I software in questione però richiedono sorgenti di traiettorie di input precise e flessibili. Per questo motivo, il Precise Orbit Propagator è stato sviluppato.

Scopo di questa Tesi è stato quello di consolidare lo sviluppo di tale Propagatore mediante l'inserimento di nuovi componenti tra i modelli di forze, unito al miglioramento dei modelli di perturbazioni già presenti tramite una più accurata descrizione dei parametri ambientali. Un ulteriore sviluppo ha riguardato l'inserimento di un processo per il controllo delle discontinuità all'interno degli integratori numerici, per limitare gli errori di integrazione incontrati in caso di manovre orbitali.

Una serie di analisi sono state effettuate per investigare l'impatto di tutte le perturbazioni sulla propagazione, in diversi regimi orbitali. I risultati hanno indicato che tutti i componenti della parte di dinamica del propagatore sono necessari per raggiungere una modellazione dell'orbita propagata inferiore al metro. Inoltre, analisi di sensibilità sono stati condotti sui modelli, evidenziando come geopotenziale e resistenza aerodinamica siano estremamente variabili a seconda della scelta dei modelli di gravità e densità atmosferica. Altre analisi hanno infine mostrato come l'inclusione del processo per il controllo di discontinuità abbia permesso di azzerare gli errori numerici introdotti dalle manovre.

Avendo raggiunto i requisiti riguardo accuratezza numerica e fedeltà della modellazione, il prossimo passo per lo sviluppo del Propagatore è la validazione finale utilizzando dati satellitari reali, dopo il quale il software avrà raggiunto il necessario grado di maturità.

Parole chiave: Propagazione Orbitale, Perturbazioni Orbitali, Precise Orbit Determination, Integrazione Numerica

Contents

1 | Introduction

1.1. Rationale and Motivation

Earth Observation satellites have been subject of a rapid and constant technological development for several decades at present time, providing unquestionable benefits to scientific progress and humankind in general, thanks to the vastness of purposes this kind of missions cover. However, with the progressive increase in performance and quality of the scientific products of such satellites, new engineering challenges have come up as well. One of the most critical aspects for ensuring a correct post-process of the scientific data is the accurate reconstruction of the satellite ephemeris, without which the scientific meaningfulness of the raw data could be jeopardized. For this reason, the requirements in this sense have grown at the same rate of the precision of the spatial products. In fact, several already flown Earth Observation missions, like the Ocean Topography mission TOPEX/Poseidon [32], the Synthetic Aperture Radar (SAR) satellite TerraSAR-X [36], and the geodetic missions GRACE and GOCE [11, 20], all require an accuracy of the orbit determination solution of cm-level.

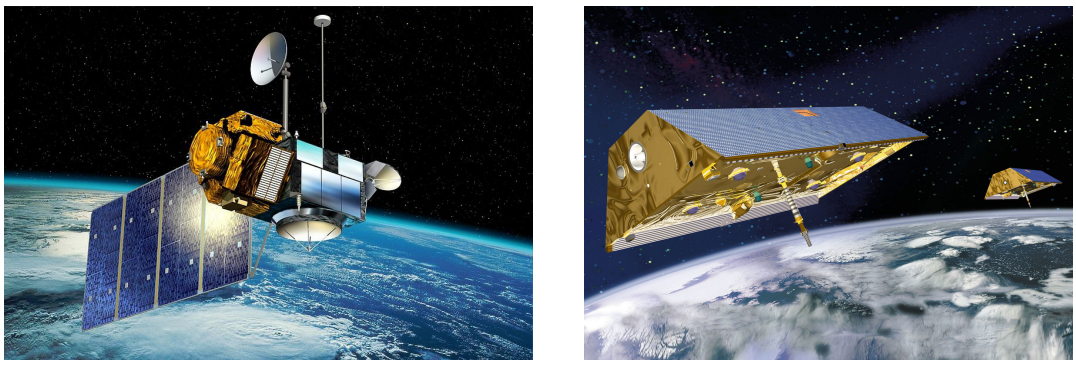

(a) TOPEX/Poseidon (b) GRACE

Figure 1.1: Notable scientific LEO missions

Since most of these Earth Observation missions fly in Low Earth Orbit, Precise Orbit Determination (POD) techniques are employed, which thanks to GNSS-based measurements

are capable of reconstructing the satellite state with sufficient accuracy [8]. Several POD techniques can be used to reach this scope, which generally span from relying sorely on the GNSS measurements (Kinematic POD) to instead using formulations based exclusively on forces predictions (Dynamic POD). One particular subset of POD techniques is the so called Reduced-Dynamic POD [37], which is essentially a tradeoff between the two, being able to adapt the amount of dynamical modelling based on the quality of the GNSS measurement and more in general on the mission scenario. On the one hand, this method increases the flexibility of the solution and allows to obtain accurate ephemeris also in case of limited GNSS visibility or poor measurements quality, but on the other hand a tuning and calibration process is required due to the presence of empirical parameters which compensate the lack of fidelity of dynamical models. To sum up, this category of POD is well-established and has allowed to obtain consistent performances satisfying the above-mentioned requirements for some already flown missions. However, most of the software solutions developed in this subject largely differ in the extent and detail with which the perturbations model are described. In addition, they were based until now on Earth observation missions with a limited number or rotational and translational maneuvers. As this is rapidly changing due to the advent of the so called Agile satellites, new software solutions are needed in the space industry to answer the extended flexibility requirement. For this reason, within AIRBUS Defence and Space in Friedrichshafen (Germany), a new tool for Reduced-Dynamic POD for LEO satellites is being developed: PODCAST (Precise Orbit Determination for Complex and Agile Satellite Technology) [7], which aims to provide a flexible testbed for novel approaches related to POD and Precise Baseline Determination (PBD) of non-agile and agile satellites. However, for appropriate testing and validation of this software, jointly with the necessity of calibrating the estimation parameters dealing with the force models, sufficiently accurate reference orbit solutions need to be employed. This means that the input trajectories provided to the estimation software must be realistic, in the sense of being sufficiently representative of real satellite motion in order to allow for an accurate calibration, and free of numerical noise. Regarding this, the input trajectory should have a numerical error which is at least one order of magnitude lower than the one of the estimation accuracy [17]. Real satellite data is often sparse, of ambiguous precision and in any case of difficult controllability, therefore a new technological solution is required. With this need in mind, the Precise Orbit Propagator (PrOP), object of this Thesis, was born, aiming to reach the capability of generating input reference trajectories with precision comparable to the one of the POD solutions. The challenges and problems the software has to face in order to fulfill its functional requirements are reported in the next section.

1.2. Problem Statement

The task of an Orbital Propagator is to retrieve the solution of the Initial Value Problem composed by the differential equations describing the Equations of Motion of the spacecraft, coupled with the satellite state initial condition. This solution or, in other terms, the propagated position and velocity, can be obtained via three main techniques: analytical, semi-analytical or numerical propagation, depending on the specific needs of the user and the available information. As a consequence of its previously state purpose, the main requirement for the Propagator developed for this Thesis is high accuracy, therefore the most suitable choice is certainly towards numerical integration, as it will be described in chapter 2.

In addition, another important need as previously mentioned is the one concerning the flexibility of the software solution. Therefore, the propagator must ensure the user of a sufficient variety of choice of propagation components, among which the numerical integrators and the force models to employ. All of these components will be described in detail in the following chapters.

However, along with the possibility of having different components combination, the awareness of the impact on the solution generated by any possible choice needs to be acquired, in order to adapt the software configuration to any possible scenario, while keeping the required performance.

Partially, this knowledge was already acquired in past analyses, specifically concerning the accuracy provided by several numerical integrators and the impact of not so common numerical techniques in the differential equation formulation, as reported in chapter 2. Nevertheless, many fundamental aspects have remained uncovered, such as the effect of the different force models on the solution. For this reason, the main question which the analysis included in this thesis aimed to answer is formulated as follows:

- *To what extent do the different dynamical models contribute to the propagation solution? And at which computational cost?*

Therefore, the Thesis main goal is to first of all describe the models and techniques implemented in the propagation software, followed by analysis of the correspondent contributions of each implementation.

1.3. Thesis Outline

This Thesis document has been structured as follows. *Chapter 2* briefly illustrates the background of numerical orbit propagation, reviews the main propagation features of some of the commonly employed commercially available softwares and collects the main results already achieved by the Precise Orbit Propagator. *Chapter 3* introduces the dynamical models implemented in the software. *Chapter 4* gives details about the constituents of the numerical propagator, discussing about the several integrators with their corresponding stepsize control, along with the numerical formulation of the Ordinary Differential Equation and the techniques which act on the floating point precision for the numerical integration that have been used. *Chapter 5* shows the results of the tests and analyses carried out to highlight the impact of each component on the propagator accuracy and efficiency. Finally, in *Chapter 6*, some conclusions of the study and future developments for the software are stated.

2 | Propagator Background

2.1. Introduction to Numerical Propagation

Given the high accuracy requirement to which the propagator is subject, numerical orbit propagation is the only suitable technique for obtaining the evolution in time of the spacecraft state, namely its position and velocity history [17].

This method aims to solve n-dimensional first order equations of the form:

$$\dot{\mathbf{y}} = \mathbf{f}(t, \mathbf{y}) \qquad \mathbf{y}, \dot{\mathbf{y}}, \mathbf{f} \in \mathbb{R}^n \tag{2.1}$$

This can be obtained starting from the relationship between the position $\mathbf{r}$ and acceleration $\mathbf{a}$, reported in eq. (2.2):

$$\ddot{\mathbf{r}} = \mathbf{a}(t, \mathbf{r}, \dot{\mathbf{r}}) \tag{2.2}$$

By defining the state vector as the combination of position and velocity:

$$\mathbf{y} = \begin{bmatrix} \mathbf{r} \\ \dot{\mathbf{r}} \end{bmatrix} \tag{2.3}$$

The original shape of eq. (2.1) can be obtained:

$$\dot{\mathbf{y}} = \mathbf{f}(t, \mathbf{y}) = \begin{bmatrix} \dot{\mathbf{r}} \\ \mathbf{a}(t, \mathbf{r}, \dot{\mathbf{r}}) \end{bmatrix} \tag{2.4}$$

However, numerical integration is affected by errors, which can be grouped in the following distinctions:

- Modeling Error: caused by the fact that the dynamical equations used to calculate the accelerations will always represent an approximation, to a certain extent, of the

real physical behaviour. It can be mitigated by using more detailed and realistic dynamical models, this however adds complexity and computational cost to the system;

- Truncation Error: intrinsic of the approximation employed by the numerical integrator to solve the differential equation. It can be mitigated by using higher order integrators and/or integrators with finer stepsize, incrementing as such the computational burden;
- Round-off Error: consequent of the finite number of digits used to carry out numerical integration and algebraic operations in general. It can be mitigated by increasing the floating point precision of the used variables.

By keeping this in consideration, and recalling the main performance requirement of propagation accuracy better or at least equal to the one of state of the art POD, it is clear that the main goal of the Propagator shall be to minimize the contribution of the errors described above.

However, this is not straightforward, as solutions which aim to mitigate one of the three errors might be detrimental to another one. A trivial example of this phenomenon involves the link between Truncation and Round-off Errors: if a higher order integrator with a finer time discretization is employed, the Truncation Error will benefit, but on the other hand, the number of algebraic operations needed increases, and therefore the Roundoff Error worsens, as depicted in fig. 2.1. It is clear that a tradeoff must be found to minimize the overall error.

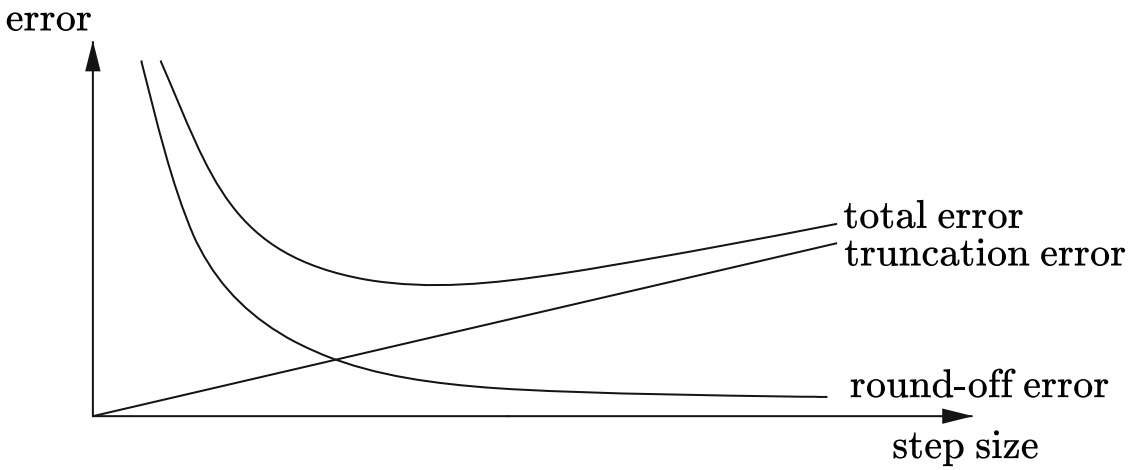

Figure 2.1: Roundoff vs Truncation Errors with varying Stepsize [15]

Furthermore, even though the computational cost is not the main requirement of this

Propagator, care shall in any case be taken upon the numerical burden introduced by the components, as they might eventually jeopardize the flexibility and well-functioning of the software.

2.2. State of the art of Numerical Orbit Propagation Softwares

Despite the fact that the Precise Orbit Propagator became to be developed in order to answer a specific need, which is to generate input trajectories for the POD software, an additional reasonable soft goal was to build it in such a way that it could be used for a wider variety of purposes and scenarios. In fact, it would be overly counterproductive to develop a tool capable of handling only a limited amount of propagation situations (e.g. very precise LEO propagation for 24 hours), forcing to use other software solutions for other not so distant case studies. Therefore, to enhance the flexibility and completeness of the tool, a quick survey on the most popular Flight Dynamics program used for Numerical Orbit Propagation was conducted.

The first analysed software was the General Mission Analysis Tool (GMAT), an open-source mission analysis program developed by the joint effort of NASA and private industry [10]. It has been used and successfully validated with several mission, including LCROSS, the Lunar Reconnaissance Orbiter, OSIRIS-REx, the Magnetospheric Multiscale Mission, and the Transiting Exoplanet Survey Satellite (TESS) mission. It is implemented in C++, using an Object Oriented methodology, and it can be driven either from an interactive Graphical User Interface (GUI), or from a custom script language. The GUI window used for the configuration of the propagator is reported in Figure 2.2.

The window appears quite compact and intuitive. The first option which can be modified is the numerical integrator to employ for the propagation, along with its related characteristics as the step size length and the tolerance level for the step size control. GMAT implements a good variety of single step integrators, spanning from the Runge-Kutta4 to the Runge-Kutta89, whereas the only multistep integrator implemented is the Adams-Bashforth-Moulton. On the right side instead the Force Model can be set up. The software implements almost all of the commonly employed dynamical models, namely the primary body gravity (including a geopotential model setup), tide models, aerodynamic drag, solar radiation pressure, third body gravity and relativistic correction. However, both the geopotential and atmospheric density models choices are quite limited, and employ outdated models. In addition, if for the former an external input in terms of coefficient file

can be provided (even though the format required does not follow any particular standard), for the latter a plug-in principle is impossible without manually coding the extra feature.

The satellite characteristics, including the initial state, surface and mass properties can be configured in a separate spacecraft configuration window. Finally, orbit control maneuvers can be configured in the Burns window, allowing to indicate the thrust vector, the frame and the relationship between the thrust and decrement of the spacecraft mass.

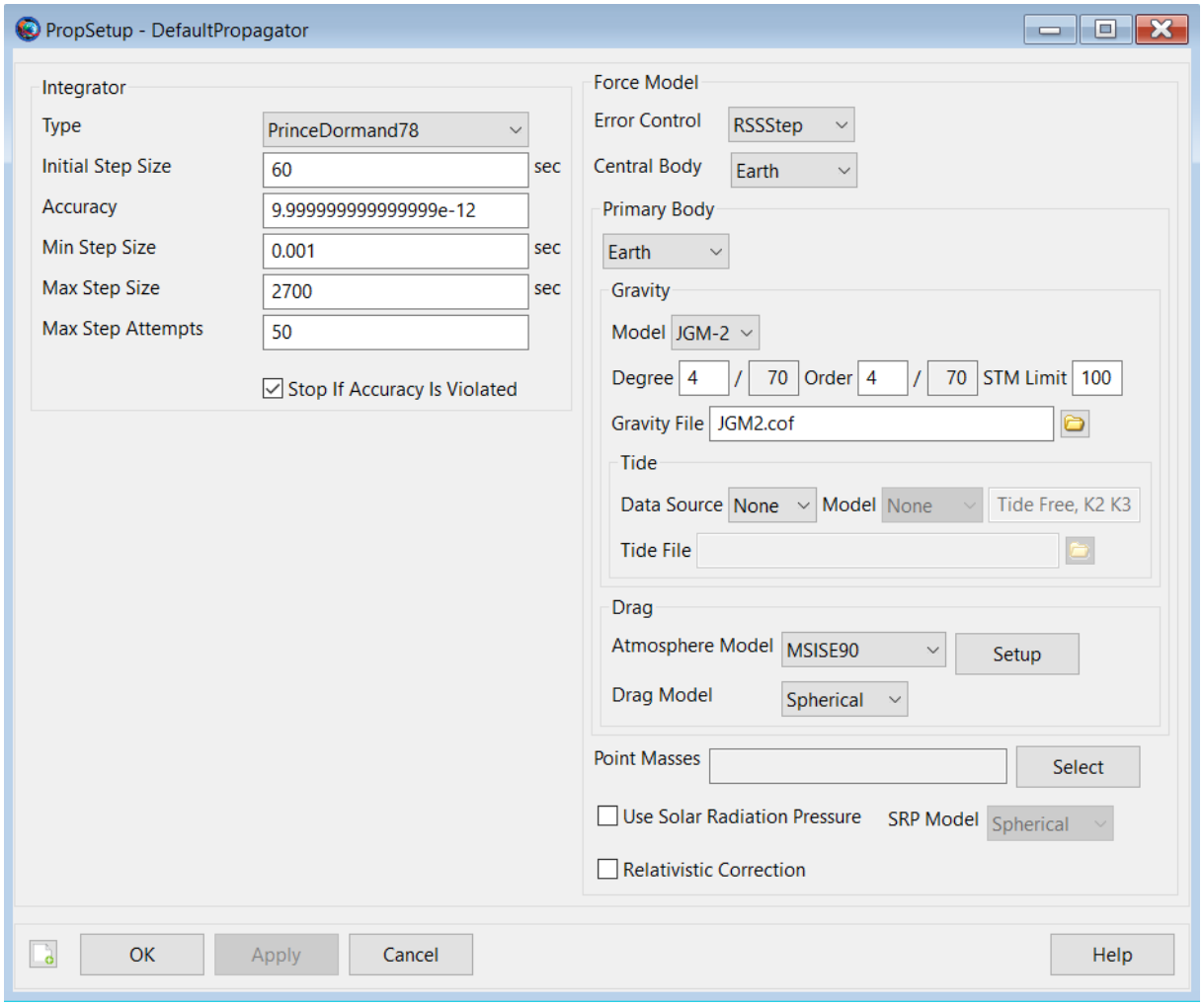

Figure 2.2: GMAT Propagator Configuration Window

The second program which was investigated was the Systems Tool Kit (STK), a multi-physics software application developed by Analytical Graphics Inc. It allows to perform complex analyses of ground, sea, air, and space platforms, and to share results in one integrated environment [2]. STK has been used by an high number of public and private institutions in the aerospace and defence sector, and has often been employed as a refer-

ence for the validation of numerical orbital simulators similar to the one developed during this thesis [24, 26, 34]. For this reason, it was decided to keep this baseline tool also for the validation part of the analyses of the thesis, specifically via the High Precision Orbit Propagator (HPOP) included in this software package.

As for GMAT, also STK offers the possibility of developing simulations both via a GUI and scripting commands. The HPOP GUI separates integrators and force models in two different windows, as seen in Figure 2.3.

In general, more options for the configuration are available in this case with respect to GMAT, as well as more updated models for the gravity and atmospheric density formulations. It is also notable that there is the possibility of including the perturbation coming from the radiation pressure of the primary body, along with the one of choosing the different shadow model for computing eclipses or the way to interpolate space weather data when using empirical models. It is clear how this potentially allows for more sophisticate analyses. For what concerns the integrator availability, this is more restricted than GMAT, but in any case the most commonly employed high order integrators for orbital propagation are present.

2.3. PrOP State of Development

This section summarizes the main implementations and results of the Precise Orbit Propagator reached prior to this Master Thesis work [31]. First of all, to satisfy the flexibility and PODCAST compatibility requirements, PrOP was developed in C++, designed with a modular architecture using the Object Oriented features of this programming language. The modular architecture allowed to easily build and extend alternatives for each of the main software components of the Propagator, as for the Force Models and the Numerical Integrators. For the Force Models in particular, a class for each perturbation was created, all of which implemented an equal common interface for the calculation of the acceleration at a particular state.

The numerical integrators that were implemented will be subject of more detailed description in chapter 4. The single step options included were: Euler, RungeKutta4, DormandPrince4(3), DormandPrince5(4), DormandPrince6(5), DormandPrince7(6), DormandPrince8(7), while the multistep integrator were: StoermerCowell, GaussJackson.

The Force Models considered were instead: acceleration due to Central Body Gravity, Geopotential acceleration, Tides, Thid Body perturbation, Aerodynamic Drag, Solar Radiation Pressure and Orbital Control Maneuvers. However, most of them used simple

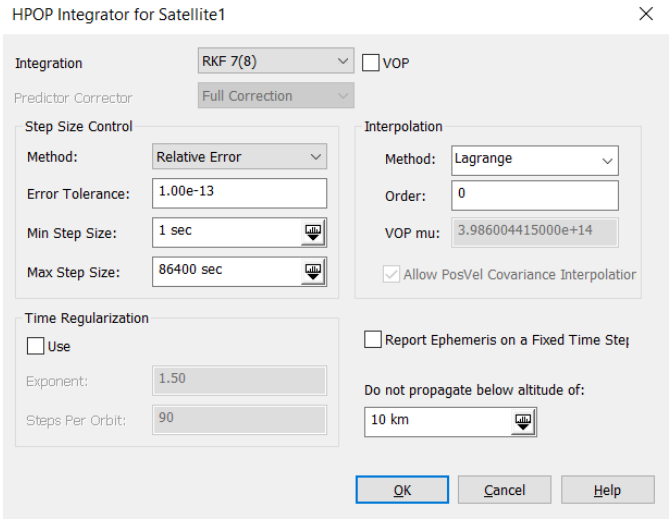

(a) Integrator Configuration

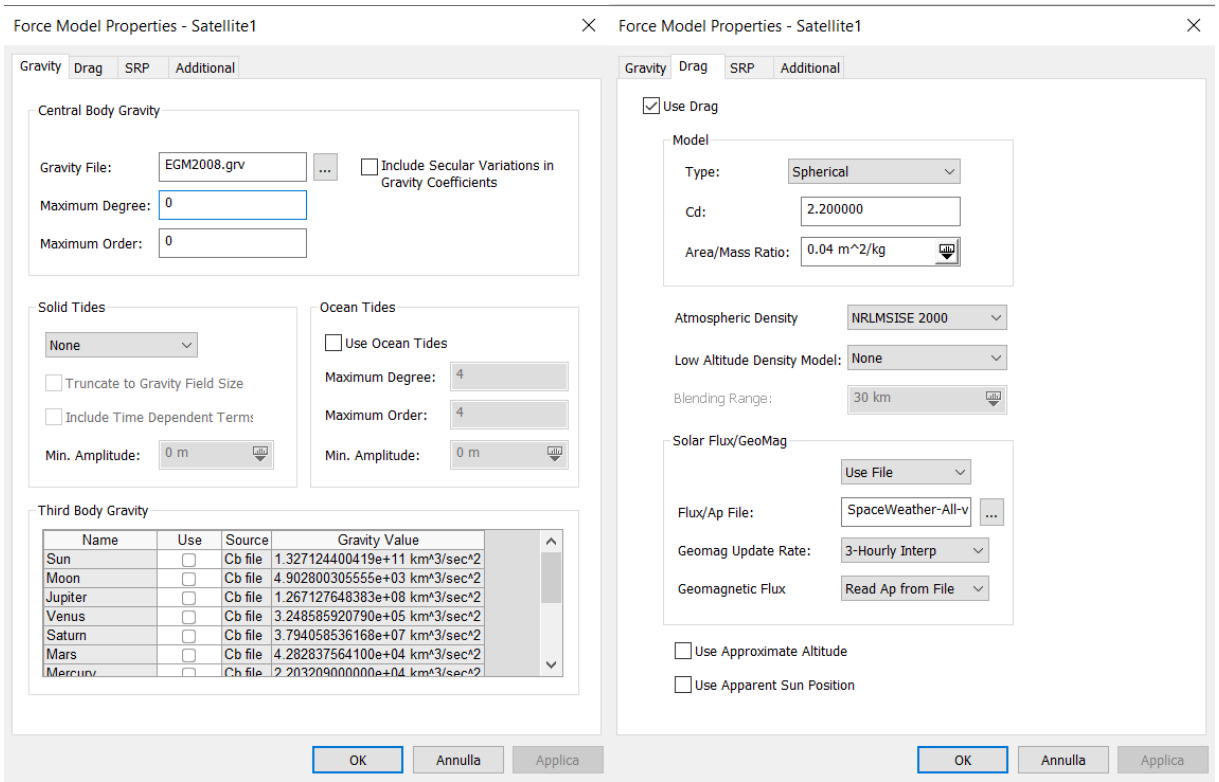

(b) Gravity Configuration

(c) Drag Configuration

Figure 2.3: STK HPOP Configuration Windows

models for their mathematical formulation, the enhancement of which is described in chapter 3. In addition, the impact of these models was not investigated at all.

Instead, the past analyses focused on researching ways to reach the numerical accuracy requirement of 10^{-4} m. This was carried out using mainly two numerical techniques, both described again in chapter 4: Hybrid precision and the Encke's formulation. The former increments the floating point precision for the storage of numerical variables in some components of the program, while the latter is an alternative way to formulate the differential equation to numerically integrate. These analyses studied the propagation solution accuracy by integrating a simple two body problem, for which the analytical solution is known, using different integrators, step sizes and including or not the Hybrid precision and Encke formulation.

These studies highlighted that the use of Hybrid precision had an higher impact on the results than the Encke's formulation. In particular, from fig. 2.4, we can see the behaviour of the Common Digits (a metric for the solution accuracy), by using the same numerical integrators with and without the Hybrid formulation, with varying step size (in the figure the number of function calls is reported, which is inversely proportional to the step size).

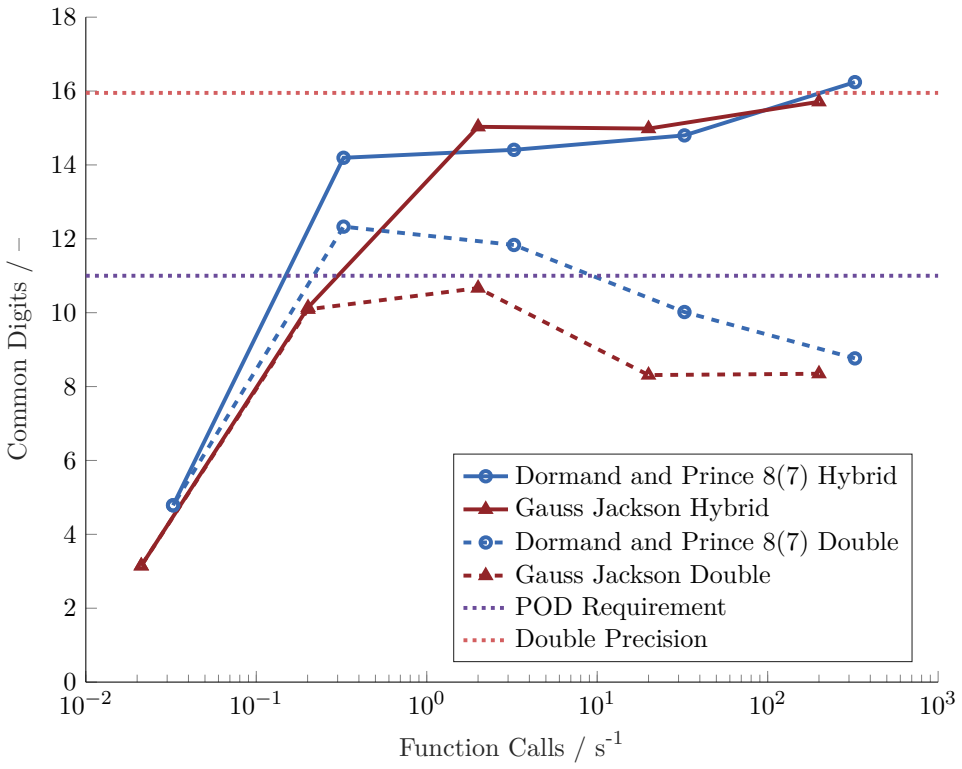

Figure 2.4: Accuracy of Integrators with Hybrid Precision [31]

While with the original Double precision, the accuracy requirement was satisfied only for

some particular values of step size due to the contrast between Truncation and Roundoff errors, with the Hybrid Precision this is no longer true. In fact, even for smaller step sizes, the roundoff error is relegated to very low digits, and therefore highly mitigated. This allowed to reach and even surpass the precision requirement. In fact, both the DormandPrince8(7) and the GaussJackson integrators, for smaller step sizes, reached an accuracy equal to the one of double precision representability, when using the Hybrid Precision.

On the other side, as we can see from fig. 2.5, the employment of the Hybrid precision caused an increase in the computational time, as expected. This increase was seen to be higher for the GaussJackson integrator.

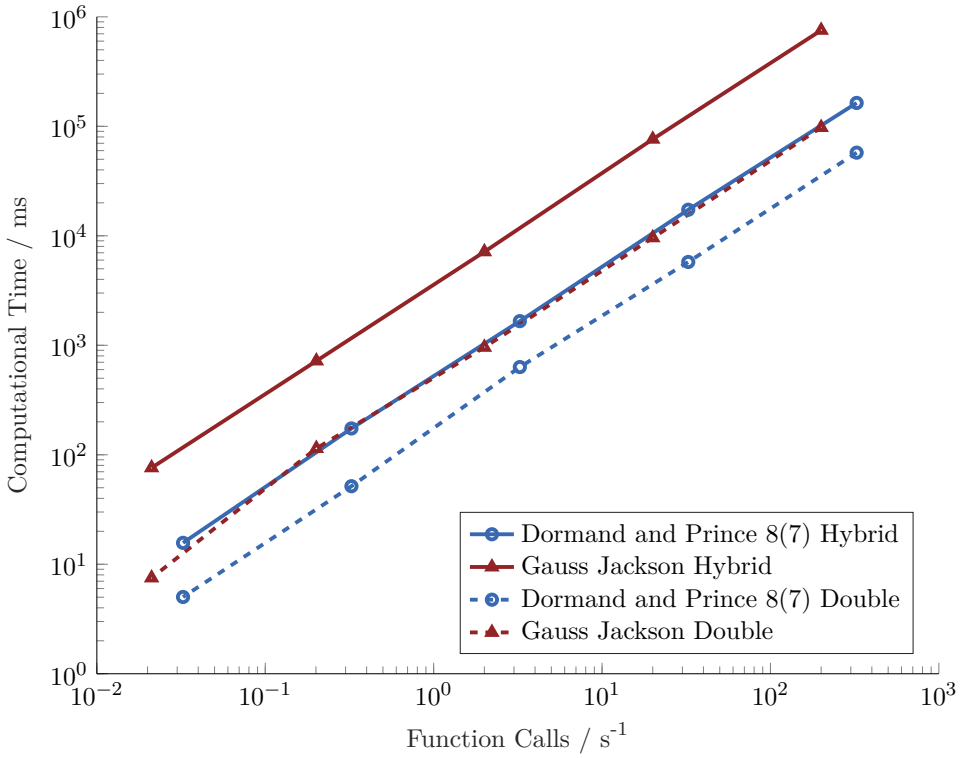

Figure 2.5: Integration Time with Hybrid Precision [31]

However, this computational time increase became only a small percentage of the global computational time when using a geopotential model, as seen in fig. 2.6, due to the higher complexity of this force model. This proved even more the power of this implementation: when considering a more complete dynamical formulation to integrate, which therefore causes high computational times, Hybrid Precision grants an higher accuracy at the cost of a relatively small computational cost increase.

For what concerns the results using the Encke's method instead, fig. 2.7 illustrates a

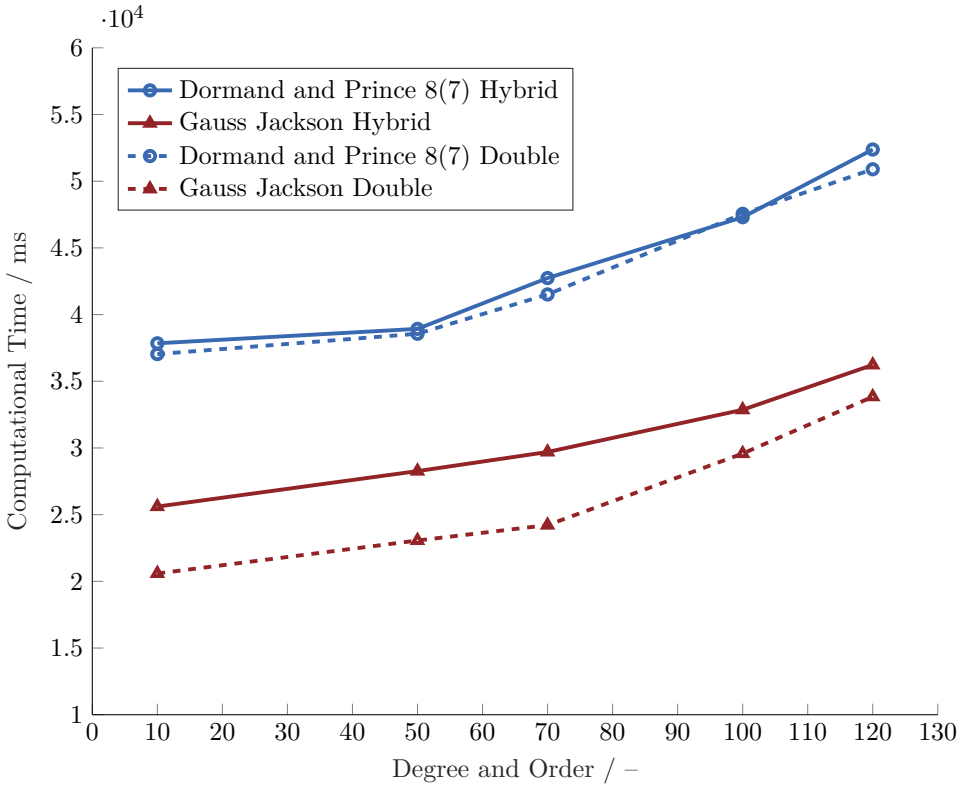

Figure 2.6: Integration Time of Geopotential with Hybrid Precision [31]

comparison of solutions acquired integrating in double precision with Encke's method the point mass force and geopotential, with a reference solution acquired integrated in hybrid precision. The increase in accuracy brought by this method is more relevant for the GaussJackson integrator, and affects mainly the step size of maximum accuracy. Overall, the improvement is less evident than the one obtained with the Hybrid Precision.

However, as can be seen in fig. 2.8, where the integration time is plotted with and without Encke's method, the increase in computational cost that this formulation introduces is negligible.

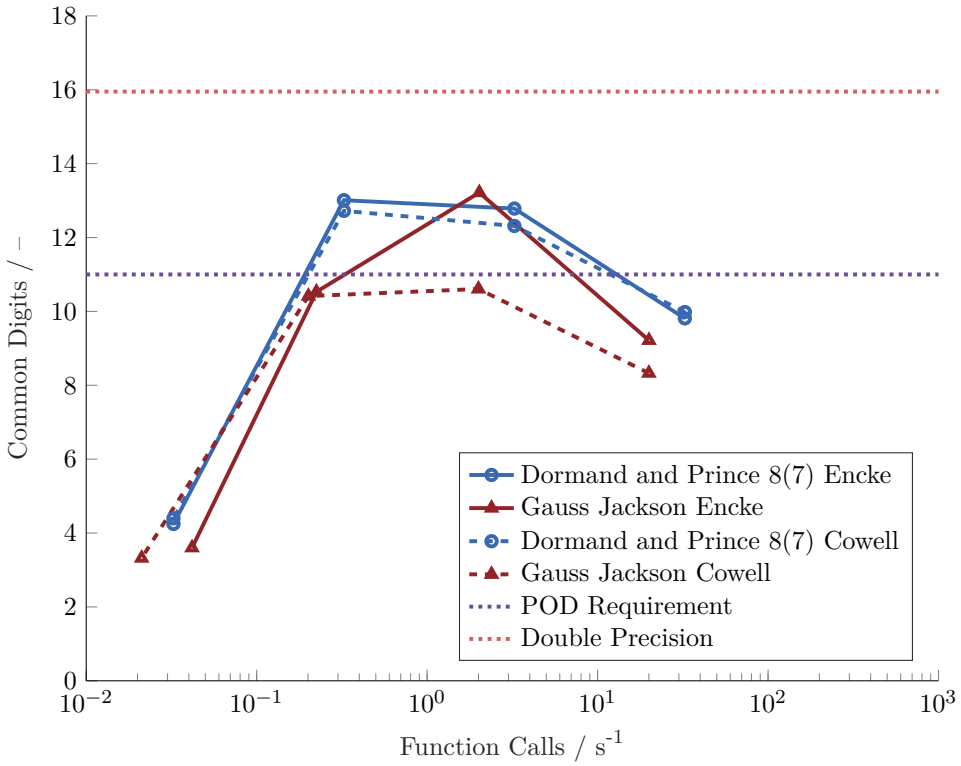

Figure 2.7: Accuracy of Integrators with Encke's method [31]

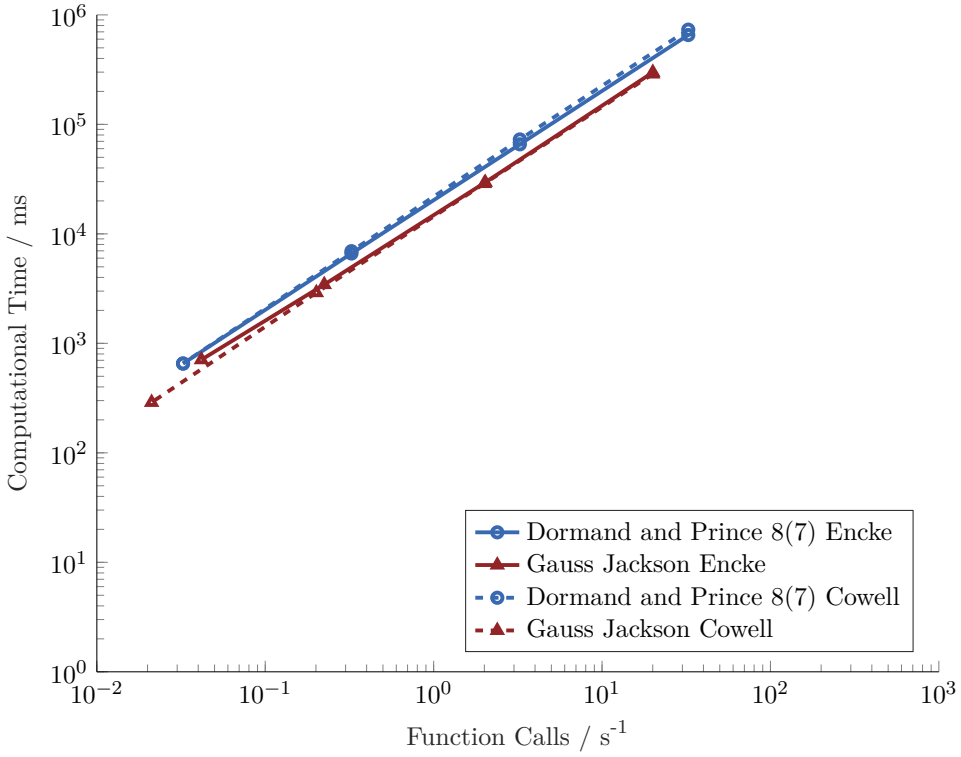

Figure 2.8: Integration Time with Encke's method [31]

3 | Dynamics Modelling

As stated in the introduction, the prediction of the state evolution of the spacecraft is obtained by integrating the equations of motion. In the framework of Newtonian physics, this translates in a second order Ordinary Differential Equation linking the acceleration experienced by the spacecraft to the total force which it is subject to, as in eq. (3.1):

$$\ddot{\mathbf{r}} = \mathbf{a} = \frac{\mathbf{F}(t, \mathbf{r}, \mathbf{v})}{m} \tag{3.1}$$

As a first approximation, the force acting on a satellite can be assumed to be exactly equal to the Earth central gravity. Approximating the Earth as a point-mass object, or a perfectly spherical object with concentric layers of constant density, the following equation is therefore obtained:

$$\ddot{\mathbf{r}} = -\frac{GM}{r^2}\hat{\mathbf{r}} \tag{3.2}$$

With GM being the gravitational parameter of the central body, and $\hat{\mathbf{r}}$ the unit position vector. This equation represents the Restricted Two Body Problem, and it has an analytical solution, often referred to as the Kepler Orbit. As the name suggests, this kind of orbits satisfy the Kepler Laws, having an elliptical shape (or in general the one of a conic) and constant geometrical properties and parameters.

However, this mathematical formulation can be far too rough for several reasons: first of all, the Earth is not a perfect sphere, having a very irregular shape and constantly varying composition, leading to a more complex gravity field expression. Furthermore, Earth gravity is the major but not the only force acting on the satellite in space.

As a result, it is clear that a more refined approach is needed in order to fulfil the previously stated precision requirements. To achieve this, a more general approach is introduced, the Perturbed Two Body Problem, reported in eq. (3.3) using the Cowell formulation:

$$\ddot{\mathbf{r}} = -\frac{GM}{r^2}\hat{\mathbf{r}} + \sum_i \mathbf{a}_i \tag{3.3}$$

Where the additional accelerations $\mathbf{a}_i$ are the effect of the orbital perturbations acting on the satellite.

By recalling the problem of the modelling error in orbital propagation, it is clearer now that this can be reduced in two ways:

1. by increasing the number of perturbations considered (i.e. increasing i), therefore taking into account as most forces as possible;
2. by using more refined models to compute the perturbing forces, in order to better represent the reality.

Within the Propagator object of this Thesis, both the approaches were implemented. The perturbations considered and their respective adopted models will be illustrated in this chapter.

A first order qualitative assessment of the order of magnitude of the major orbital perturbations as a function of the Orbit Altitude is illustrated in fig. 3.1.

It has to be noted that almost all the perturbations arise due to some sort of interaction between the spacecraft and the surrounding environment. As a consequence, more advanced perturbation modelling requires better environmental models. Due to the variety of applications of this research topic, an extremely high amount of environmental models have been developed throughout the decades, therefore some sort of guidelines need to be established in order to be able to choose the most adequate models. To this aim, the ECSS-E-ST-10-04C document [1], describing the requirements for Space Environment description, has been taken as a reference. Specific comments regarding the ECSS regulations will be reported in the respective dynamical models paragraphs.

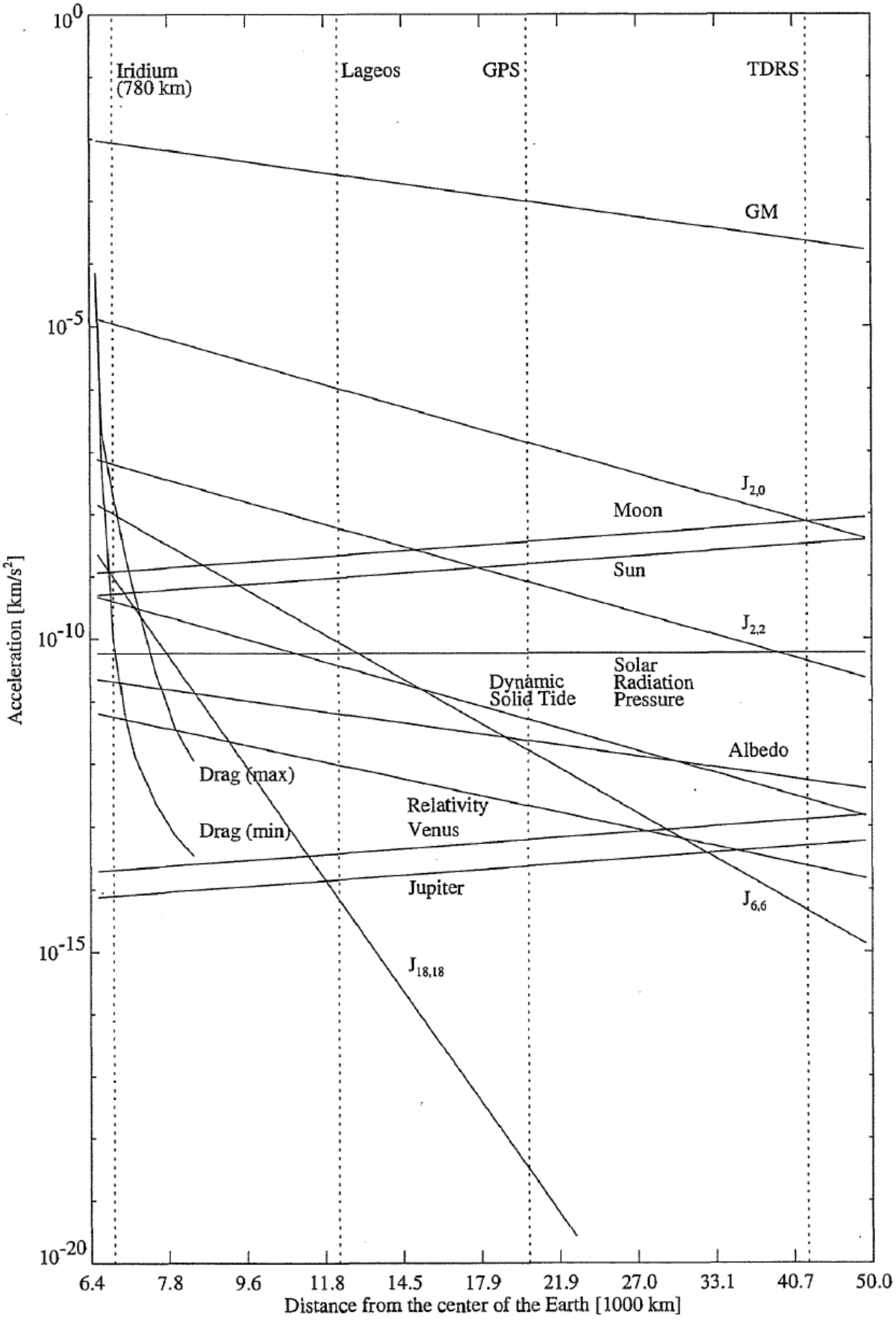

Figure 3.1: Orders of Magnitude of Perturbations

3.1. Earth Gravity Modelling

The attraction force generated by the Earth gravity field is the primary force to which Earth orbiting satellites are subjected to. As such, lack of gravity modelling accuracy can cause very large errors in the acceleration computation. The central gravity force previously reported shall then be complemented by an extended formulation which takes into account the irregular shape and composition of the Earth. To do so, the potential of the field, U, is exploited, which satisfies the Laplace equation:

$$\nabla^2 U = 0 \tag{3.4}$$

The resulting acceleration can then be computed as the gradient of such potential:

$$\ddot{\mathbf{r}} = \nabla U \tag{3.5}$$

In case of the central gravity force then, the potential takes the following form:

$$U = \frac{GM}{r} \tag{3.6}$$

However, in the more general case, a more advanced formulation is used to describe the gravity potential as a function of a set of three spherical coordinates (r, ϕ, λ), namely the geocentric distance, geodetic latitude and longitude, using a spherical harmonics expansion, as in eq. (3.7):

$$U = \frac{GM}{r} \sum_{n=0}^{\infty} \sum_{m=0}^{n} \frac{R^n}{r^n} P_{nm}(\sin\phi)(C_{nm}\cos(m\lambda) + S_{nm}\sin(m\lambda)) \tag{3.7}$$

Where P_{nm} is the associated Legendre polynomial of degree n and order m, defined as:

$$P_{nm}(u) = \frac{(-1)^m}{2^n n!}(1-u^2)^{m/2}\frac{d^{m+n}}{du^{m+n}}(u^2-1)^n \tag{3.8}$$

The coefficients C_{nm}, S_{nm} instead describe the dependence on the internal mass distribution of the Earth. Coefficients associated to $m = 0$ are called zonal coefficients, as they describe the part of the geopotential not dependent on longitude. Coefficients with $m < n$ and $m = n$ are instead defined as tesseral and sectorial coefficients, respectively.

However, due the fact that for the vast majority of gravity models those coefficients are

characterized by an high variability in terms of magnitude when varying the indices m, n, a normalization is often applied to make them more uniform than unnormalized coefficients, by using the normalization factor reported in eq. (3.9):

$$N_{nm} = \sqrt{\frac{(n+m)!}{(2-\delta_{0m})(2n+1)(n-m)!}} \tag{3.9}$$

Therefore, the normalized coefficients are computed as:

$$\bar{C}_{nm} = N_{nm} C_{nm} \quad , \quad \bar{S}_{nm} = N_{nm} S_{nm} \tag{3.10}$$

While the associated Legendre polynomials are normalized with the inverse of N_{nm} :

$$\bar{P}_{nm} = \frac{P_{nm}}{N_{nm}} \tag{3.11}$$

For practical purposes, the series expansion is truncated after a certain number of terms N, the maximum order of the model. The definitive potential expression is finally reported in eq. (3.12):

$$U = \frac{GM}{r} \sum_{n=0}^{N} \sum_{m=0}^{n} \frac{R^n}{r^n} \bar{P}_{nm}(\sin\phi)(\bar{C}_{nm}\cos(m\lambda) + \bar{S}_{nm}\sin(m\lambda)) \tag{3.12}$$

Computing the analytical gradient of the potential as expressed in eq. (3.12) can be quite cumbersome and computationally unfeasible. To avoid this, some particular properties of the associated Legendre polynomials and coefficients are usually exploited to reach less demanding recursive expressions. For the present work, the formulation of Montenbruck and Gill [17] was used to compute the geopotential acceleration, for which the most relevant expressions are reported for the sake of completeness.

Therefore, two functionals are defined:

$$\begin{aligned} V_{nm} &= \left(\frac{R}{r}\right)^{n+1} P_{nm}(\sin\phi)\cos m\lambda \\ W_{nm} &= \left(\frac{R}{r}\right)^{n+1} P_{nm}(\sin\phi)\sin m\lambda \end{aligned} \tag{3.13}$$

As already stated, thanks to the properties of the Legendre polynomials and the trigonometric functions, functionals of eq. (3.13) can be easily calculated with recursive formulas

which do not even require conversion from cartesian to spherical coordinates [17].

Finally, the acceleration components may be computed as in eq. (3.14):

$$\ddot{x} = \sum_{n,m} \ddot{x}_{nm} \quad , \quad \ddot{y} = \sum_{n,m} \ddot{y}_{nm} \quad , \quad \ddot{z} = \sum_{n,m} \ddot{z}_{nm} \tag{3.14}$$

Where the summation terms are obtained via the following relations:

$$\begin{aligned} \ddot{x}_{nm} &\overset{(m=0)}{=} \frac{GM}{R^2}\{-C_{n0}V_{n+1,1}\} \\ &\overset{(m>0)}{=} \frac{GM}{2R^2}\Big\{(-C_{nm}V_{n+1,m+1} - S_{nm}W_{n+1,m+1}) \\ &\quad + \frac{(n-m+2)!}{(n-m)!}(C_{nm}V_{n+1,m-1} + S_{nm}W_{n+1,m-1})\Big\} \end{aligned} \tag{3.15}$$

$$\begin{aligned} \ddot{y}_{nm} &\overset{(m=0)}{=} \frac{GM}{R^2}\{-C_{n0}W_{n+1,1}\} \\ &\overset{(m>0)}{=} \frac{GM}{2R^2}\Big\{(-C_{nm}W_{n+1,m+1} + S_{nm}V_{n+1,m+1}) \\ &\quad + \frac{(n-m+2)!}{(n-m)!}(-C_{nm}W_{n+1,m-1} + S_{nm}V_{n+1,m-1})\Big\} \end{aligned} \tag{3.16}$$

$$\ddot{z}_{nm} = \frac{GM}{R^2}\{(n-m+1)(-C_{nm}V_{n+1,m} - S_{nm}W_{n+1,m})\} \tag{3.17}$$

Note that the acceleration components calculated in eq. (3.14) are reported in an Earth-fixed frame. Therefore, a frame conversion from Earth-fixed to inertial will be needed.

3.1.1. Geopotential Model

By recalling eq. (3.12), it is possible to identify a set of independent variables which characterise a specific gravity model: the body gravitational parameter GM, the body radius R, and the coefficients $\bar{C}_{nm}$, $\bar{S}_{nm}$. Regarding the gravity model to employ for Earth orbits, the ECSS prescribes some general requirements, here briefly reported [1]:

1. The model shall be global and static;
2. The model shall be based on Grace or GOCE data;
3. The model shall be published at: `http://icgem.gfz-potsdam.de/tom_longtime`;
4. The model shall be described by spherical harmonic coefficients up to at least degree and order of 70.

One of the most commonly employed models which satisfy the above requirements is EGM2008 [19]. EGM2008, initially based on the ITG-GRACE03S GRACE-only gravitational model, is complete to degree and order 2159, and contains additional spherical harmonic coefficients up to degree 2190 and order 2159. The correspondent gravitational constant and equatorial radius assumed by the model are respectively: $GM = 398600.4415\ km^3/s^2$, $R = 6378136.3\ m$. This model is also used in IERS Conventions 2010 as the baseline for the definition of a conventional geopotential model [22].

However, even though a high number of coefficients is available, for most space applications a truncated version of the formulation can be safely employed, in order to avoid excessive computational overhead. In fact, studies suggest that a truncation at order 90 could guarantee a 3-dimensional orbit accuracy of less than 0.5 mm even for Low Earth Orbit satellites [22], for which higher-order terms of the geopotential have a non-negligible magnitude. As a matter of fact, the gravity field attenuation is more pronounced for high-degree coefficients [21].

For these reasons, EGM2008 was the first Geopotential model adopted within the Propagator, limiting the maximum degree and order to 200, to limit the computational burden resulting from the recursive equations previously reported.

However, this kind of completely static gravity models assume an immutable Earth gravitational field in time. This is indeed an approximation, as the Earth mass, structure and shape is continuously changing due to the effect of other Solar System bodies and general internal phenomena, hence causing a decrease in accuracy of constant gravitational field formulations. The former effects are modelled with the Tides, as explained in the next sections, while the latter come from peculiar modifications acting on a planetary-scale, as for

instance non-linear trends in polar regions due to accelerating ice mass loss. This kind of effects are nowadays took into account in Time-Varying Geopotentials (TVG). TVG models, along with the global static (mean) field, provide information about the secular drifts and seasonal variation trends, allowing for a more accurate gravity computation. This became possible thanks to the measurements collected during highly advanced Geodesy missions, among which particularly notable is GRACE [33], and its follow-on mission GRACE-FO [14].

For what concerns the order of magnitude of the variations introduced by these models, this of course depends on the orbit altitude. However, for Low Earth Orbits, most assessment studies seem to agree on an average orbit displacement with respect classical models of at most 3 mm/year [21, 28]. If this value could somewhat be considered negligible, it is reminded that the extremely strict orbit determination requirements of some missions (e.g. ocean topography satellites), make TVG an important component of the POD of LEO satellites.

Due to this, it was decided to build the propagator in such a way that also time-varying fields could be used. As a baseline solution to test the time-varying functionalities, the recent GOCO06s model was adopted [13].

GOCO06s is the latest release of the series of Gravity Field models developed and published by the Gravity Observation Combination (GOCO) consortium. It is a satellite-only model, i.e. it only employs measurements collected by gravity recovery spacecrafts. In particular, it is based on over a billion observations acquired over 15 years from 19 satellites (among which GRACE and GOCE are found) with different complementary observation principles, to combine high accuracy and good spatial resolution, which result in coefficients up to degree and order 300.

Thanks to the long observation period, secular and periodic variations of the field can be inferred from the measurements. This translates into a temporal variation of the normalized spherical harmonic coefficients, which can be computed at a generic time t as follows:

$$\begin{aligned}\bar{C}_{nm}(t) &= C_{nm,0} + C_{nm,trnd}\left(\frac{t-t_0}{T}\right) \\ &+ C_{nm,acos}\cos\left(2\pi\frac{t-t_0}{T}\right) + C_{nm,asin}\sin\left(2\pi\frac{t-t_0}{T}\right)\end{aligned} \tag{3.18}$$

$$\begin{aligned}\bar{S}_{nm}(t) &= S_{nm,0} + S_{nm,trnd}\left(\frac{t-t_0}{T}\right) \\ &+ S_{nm,acos}\cos\left(2\pi\frac{t-t_0}{T}\right) + S_{nm,asin}\sin\left(2\pi\frac{t-t_0}{T}\right)\end{aligned} \tag{3.19}$$

Where $C_{nm,0}$, $S_{nm,0}$ are the coefficients of the static part of the field, $C_{nm,trnd}$ and $S_{nm,trnd}$ are the coefficients of the linear trend, and $C_{nm,acos}$, $C_{nm,asin}$, $S_{nm,acos}$, $S_{nm,asin}$ indicate the coefficients for the periodic annual variations of the field.

In addition, the reference epoch t_0 is taken as the 1^{st} January 2010, while T is the annual period (365.25 days).

3.1.2. Earth Tides

The gravitational forces exerted by the Sun and the Moon on the Earth come into a variety of effects, referred as tides. Probably the most known phenomenon associated to these effects is the movement of water masses due to these external gravitational influences. These movements are called Ocean Tides. Moreover, considering that the Earth is not a perfectly rigid body, also the solid mass of the Earth is subject to deformation, both elastic and anelastic, caused by the gravitational forces, the effect of which can be even greater than the ocean tides by one order of magnitude for satellites orbiting at low altitudes [17]. These deformations on the solid body of the Earth are instead referred as Solid Earth Tides. Finally, another effect, the Pole Tide, is induced by the fact that the rotational axis of the Earth in general is not fixed with respect to the crust. This movement influences the direction of the centrifugal force experienced by the solid and water masses, which is also the responsible of the oblateness of the planet. All these phenomena contribute to adding further degrees of time-dependent variability of the Earth overall mass distribution, and therefore to the global gravity field of the planet.

The ECSS standards prescribe the use of the gravitational effect formulation related to these tides as reported in the IERS Conventions [1], therefore the Propagator tides management module was based on that particular document.

In particular, the IERS conventions relate the tidal movements to variations of the Geopotential spherical harmonic coefficients $\Delta\bar{C}_{nm}$, $\Delta\bar{S}_{nm}$. However, being the result of a long and tedious mathematical formulation, the expressions leading to the computation of these parameters is omitted for simplicity.

3.2. Third-body perturbations

The direct effect of the gravitational forces exerted by external bodies on the spacecraft can be easily computed using Newton's law of gravity, assuming the perturbing body to be a point-mass object of mass M_b, as in eq. (3.20):

$$\ddot{\mathbf{r}} = GM_b \frac{\mathbf{r_b} - \mathbf{r}}{|\mathbf{r_b} - \mathbf{r}|^3} \tag{3.20}$$

Where $\mathbf{r_b}$ is the position vector of the perturbing body in an inertial geocentric reference frame.

However, it must be noted that according to the above expression, the Earth itself would be subject to the perturbing acceleration, in this case equal to the value in eq. (3.21), hence being not at rest.

$$\ddot{\mathbf{r}} = GM_b \frac{\mathbf{r_b}}{|\mathbf{r_b}|^3} \tag{3.21}$$

This is conflicting with the overall assumption of the inertial reference frame used for the spacecraft propagation, therefore eq. (3.20) needs to be modified accordingly to ensure consistency. The final result of this modification is reported in eq. (3.22):

$$\ddot{\mathbf{r}} = GM_b \left(\frac{\mathbf{r_b} - \mathbf{r}}{|\mathbf{r_b} - \mathbf{r}|^3} - \frac{\mathbf{r_b}}{|\mathbf{r_b}|^3} \right) \tag{3.22}$$

It is clear that this formulation requires information about the positions and mass parameters of the celestial bodies of interest. In this regard, the choice adopted for the Propagator once again followed the guidelines of ECSS [1].

In particular, the position vectors of the bodies were computed using the ephemerides provided by NASA's Jet Propulsion Laboratory, the Development Ephemerides DE-430 and Lunar Ephemerides LE-430 [6]. These are a series of publicly available ephemerides in the form of Chebyshev approximations [1].

Concerning the planetary mass values instead, the results reported in the IERS Conventions were employed. These are listed in table 3.1.

	GM_i $[km^3/s^2]$
Sun	$1.32712442099 \cdot 10^{17}$
Mercury	22032.090000
Venus	324858.592000
Moon	4902.800076
Mars	4902.800076
Jupiter	126712764.800000
Saturn	37940585.200000
Uranus	5794548.600000
Neptune	6836535.000000
Pluto	977.000000

Table 3.1: Mass Parameters of Solar System Bodies [22]

3.3. Aerodynamic Drag

The aerodynamic drag generated by the interaction between the spacecraft motion and the residual atmosphere of the Earth constitutes the largest non-gravitational perturbation acting on low altitude satellites [17]. In addition, due to the way it acts, which is in direction opposite to the velocity, and belonging to the orbital plane, it constantly reduces the semi-major axis, therefore representing the major constraint on the lifetime of LEO spacecrafts. As such, the modelling of this force is critical for this kind of satellites. Nevertheless, drag is probably the most difficult perturbation to describe accurately, due to the combined uncertainties in all the parameters used for the computation of the acceleration.

The most commonly employed formulation for the computation of the acceleration caused by the aerodynamic force is reported in eq. (3.23):

$$\ddot{\mathbf{r}}_{drag} = -\frac{1}{2} C_D \frac{A}{m} \rho \; {v_r}^2 \; \mathbf{e}_v \tag{3.23}$$

Where C_D is the drag coefficient, $\frac{A}{m}$ is the ratio between the cross sectional area and the mass of the satellite, ρ is the atmospheric density, v_r is the relative velocity between the spacecraft and the surrounding air particles, $\mathbf{e}_v = \dfrac{\mathbf{v}_r}{v_r}$ is the unit vector of such relative velocity.

Each of these four parameters is characterized by some difficulties and uncertainties in its formulation.

Starting with the drag coefficient, this is a dimensionless parameter influenced by the interaction of the satellite surface with the atmospheric constituents. Typical values of this coefficient range from 1.5 - 3.0 [17]. However, because of the difficulties in the predictions of such quantity, it is usually estimated during orbit determination. For PrOP, a simple option providing a constant coefficient for the whole propagation time was implemented. Nevertheless, more advanced formulations, dealing with variations depending on the angle of attack, could be included in the future [29].

The cross section area computation usually depends on information about the attitude. Moreover, for the modelling of the spacecraft surfaces different levels of detail could be adopted. The Propagator implemented two alternatives in this regard. The first option consisted in the simple assumption of spherical surface, having a projected area value independent from the angle of attack. The more sophisticated option involved the use of a particular tool developed within AIRBUS, which starting from 3D CAD models of a particular spacecraft, generated lookup tables with the values of projected areas for a certain grid of angle of attack values. The latter was employed for all non-conservative forces analyses.

Both the density and the velocity between satellite and air depend on the complex atmosphere dynamics, therefore they will be treated in specific sections.

3.3.1. Atmospheric Density

The atmospheric density is probably the most crucial parameter for the computation of the aerodynamic drag. This is influenced by a variety of factors, including location, epoch, but even solar and geomagnetic activity levels. However, given the great interest not only for satellite missions, from the advent of the space age an incredible amount of numerical models for this environmental parameter have been developed.

The first reference models assumed a simple decreasing exponential for the formulation of the density, as in the US Standard Atmosphere 1976 [18].

However, the increase in the number of space missions with better accelerometers, allowed to develop models with higher fidelity, along with improved spatial and temporal resolutions, at the cost of an increased complexity in the mathematical formulation.

In this regard, the main requirements of the ECSS Standard are [1]:

- The NRLMSISE-00 model shall be used for calculating the neutral temperature, the total density and the detailed composition of the atmosphere.
- The JB-2006 model or JB-2008 model may be used for calculating the total atmospheric density above an altitude of 120 km.

To be compliant, both the NRLMSISE-00 and JB-2008 models were implemented, along with another recent empirical one, the DTM2020. All of these, which will be briefly introduced in this section, have used historical measurements, both space-based and ground-based, to fit the parameters of the mathematical formulation for the atmospheric constituents number density.

The NRLMSISE-00 model was a major upgrade of the Mass Spectrometer Incoherent Scatter Radar (MSIS-class) models of composition, total mass density, and temperature of the atmosphere [23]. Among the inputs, solar and geomagnetic activity indices need to be provided, in the form of F10.7 and Ap indices. The F10.7 index is a proxy used as an indicator of solar activity, and it is computed by measuring the solar radio flux at the wavelength of 10.7 cm. Instead, the Ap index provides a daily average level of geomagnetic activity. It can be obtained through a nonlinear relation with another common geomagnetic proxy, the Kp index. A notable model update, apart from the extension of the dataset used for the parameter fitting, is the introduction of the modelling for a new atmospheric component: the anomalous oxygen. This was included to correct the model estimates of total density at high altitudes (near the exobase), and it has a non negligible impact as atomic oxygen can dominate drag under particular conditions [23].

The Jacchia-Bowman 2008 empirical density model was developed as an improved revision of the Jacchia-Bowman 2006 model, based instead on the long legacy of the Jacchia models series [3]. A major relevant change with respect to previous versions was in the input indices used for the computations. In fact, to model the thermospheric heating in the solar Extreme Ultraviolet (EUV), Far Ultraviolet (FUV) and Medium Ultraviolet (MUV) regions, which influence the value of the exospheric temperature, the indices S10, M10 and Y10 have been included in the formulation along with the already present F10 index. In particular, the S10 index measure the EUV solar emission in the wavelength region of 26-34 nm, the M10 index derives from measurements of MUV radiation at 280 nm, and Y10 is a mixed index which includes effects from solar X rays at 0.1 - 0.8 nm and from EUV/FUV spectral regions. In addition, variations of the global density caused by geomagnetic storms was greatly enhanced thanks to the inclusion of a new index, Dst. The Dst (Disturbance Storm Time) is a geomagnetic index used in external magnetic field model computations. It describes variations in the equatorial ring current and is derived

from hourly scalings of low-latitude horizontal magnetic variation.

Apart from the two models recommended by the ECSS Standards, a Literature Review highlighted the existence of another very recent model, the DTM2020, which was therefore also implemented in the Propagator. This was the latest update of the Drag Temperature Model series, developed in the framework of the Space Weather Atmosphere Models and Indices (SWAMI) project, which was a European Union Horizon 2020 Framework project [4]. Again, the dataset used for the calibration of the model parameters was increased, adding very precise density data thanks to the measurements of CHAMP, GOCE and Swarm A. An interesting result is a visible decrease in the average computed density between 20% and 30% with respect to the above mentioned models, but this is in agreement with other recent empirical model releases. DTM2020 was published in two different products: the Operational and Research configurations. The former used as inputs the well established F10 and Kp indices for the solar and geomagnetic activities indication, whereas the latter introduced as proxies the more recent F30 index, which is the measurement of the solar radio flux at 30 cm wavelength, and the new planetary geomagnetic index Hp60. Even though both the F30 and Hp60 indices are still not completely accredited for an operational environment due to their recent developments, the Research release of the DTM2020 model showed the best results in terms of density fitting for the dataset considered [4].

3.3.2. Atmospheric Wind

The relative velocity between the spacecraft and the surrounding air depends both on the velocity of the satellite itself and the one resulting from the atmosphere dynamics. While the former is easily retrieved by the satellite state vector, the latter is, as the atmospheric density, not easily calculated.

In this sense, a reasonable approximation, which is also the most commonly employed formulation, is to assume that the atmosphere co-rotates with the Earth. This leads to a relative velocity formula as seen in eq. (3.24):

$$\mathbf{v}_r = \mathbf{v} - \boldsymbol{\omega}_\oplus \times \mathbf{r} \tag{3.24}$$

Where $\boldsymbol{\omega}_\oplus$ is the Earth's angular velocity vector due to its rotation motion. Maximum observed deviations from this assumption are of the order of 40%, leading to uncertainties in the drag force of less than 5% [17]. However, for more precise formulations, a term comprising the atmospheric winds has to be added, as in eq. (3.25):

$$\mathbf{v}_r = \mathbf{v} - \boldsymbol{\omega}_\oplus \times \mathbf{r} + \mathbf{v}_w \tag{3.25}$$

Empirical models based on atmospheric observations have been developed for computing this additional term, too. In this sense, the main reference for the upper atmospheric air circulation patterns is the series of Horizontal Wind Model (HWM), which is also recommended by the ECSS Standards Document [1]. The latest release of this model series, HWM14, has been implemented in the propagator. As for the empirical density models, also HWM models use the solar and geomagentic activity indices F10 and Ap [5].

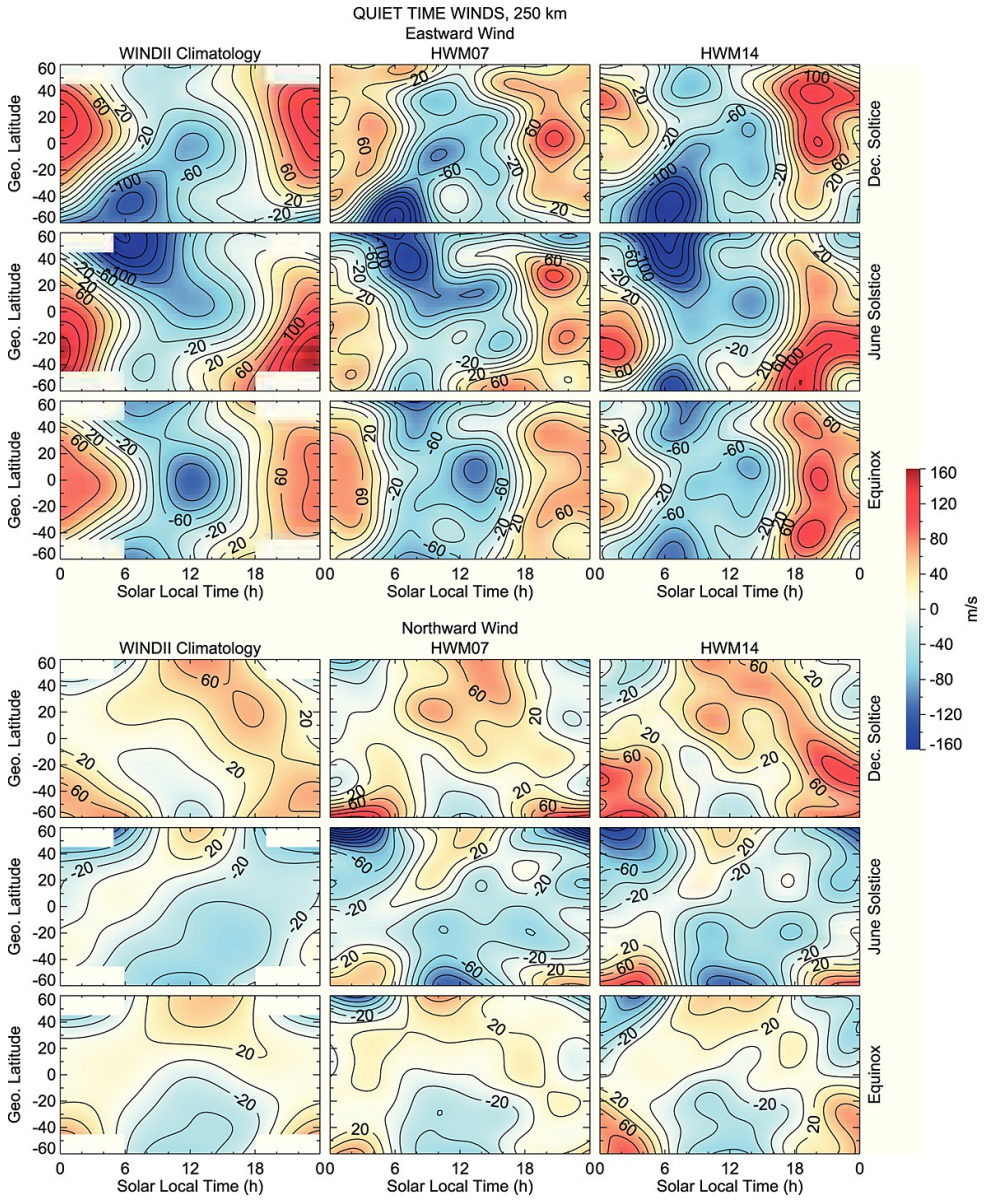

Figure 3.2: Zonal (top) and meridional (bottom) average quiet time (Kp<3) winds at 250 km altitude, as a function of solar local time and geographic latitude [5]

3.4. Solar Radiation Pressure

The photons constituting the solar radiation, when hitting the illuminated spacecraft, transfer their momentum to the satellite surfaces. This impulse generates a force acting upon a surface, or in other words, a pressure. For the case of the Sun as illuminating source, this is called Solar Radiation Pressure (SRP). SRP, as Aerodynamic Drag, is a non-conservative perturbation, and can even become the most relevant force acting on high altitude satellites, after gravity effects. For this reason, its precise modelling is crucial for the accuracy of the propagation.

The solar radiation pressure can be computed as in eq. (3.26):

$$P_{\odot} = \frac{\Phi_{\odot}}{c} \tag{3.26}$$

Where $\Phi_{\odot}$ is the solar emitted flux, whose average value is 1367 Wm^{-2}, and c is the speed of light.

The most classic formulation of this force models assumes that the photons hitting the satellite surface can either be absorbed or reflected by it [17]. Reflection can either be diffuse or specular. For the successive treatment, diffuse reflection will be neglected.

The relative importance of these modes of interaction is quantified by the optical coefficients of the surface, which depend on the material. These are the absorbivity α and the reflectivity ϵ. They satisfy eq. (3.27):

$$\alpha + \epsilon = 1 \tag{3.27}$$

Absorbed photons transfer all their momentum to the impacting surface, therefore the resulting force is directed along their direction of motion, which is opposite to the satellite-Sun direction. This force can therefore be written as in eq. (3.28):

$$\mathbf{F}_{abs} = -P_{\odot} \cos(\theta_{\odot}) A \mathbf{e}_{\odot} \tag{3.28}$$

Where $\theta_{\odot}$ is the angle between the surface normal direction and the vector direction of the Sun as seen by the spacecraft, $\mathbf{e}_{\odot}$.

As the name suggests, specular reflection implies that impinging photons are reflected in a specular direction. This momentum change of direction generates a global force which

is directed opposite to the normal direction of the surface, as seen in eq. (3.29):

$$\mathbf{F}_{refl} = -2P_{\odot}\cos(\theta_{\odot})A\cos(\theta_{\odot})\mathbf{n} \tag{3.29}$$

Combining these two forces, weighted with their correspondent optical coefficients, eq. (3.30) is reached:

$$\mathbf{F}_{SRP} = -P_{\odot}\cos(\theta_{\odot})A\left[(1-\epsilon)\mathbf{e}_{\odot} + 2\epsilon\cos(\theta_{\odot})\mathbf{n}\right] \tag{3.30}$$

However, as the solar flux which reaches a surface varies with the distance from the Sun, the SRP value is not constant in time. In particular, given the eccentricity of the Earth orbit around the Sun, variations in the SRP value of up to 3% are experienced over the year. By introducing this variation with the distance from the Sun, the acceleration due to SRP can finally be computed as in eq. (3.31):

$$\ddot{\mathbf{r}}_{SRP} = -P_{\odot}\frac{1AU^2}{r_{\odot}^2}\frac{A}{m}\cos(\theta_{\odot})\left[(1-\epsilon)\mathbf{e}_{\odot} + 2\epsilon\cos(\theta_{\odot})\mathbf{n}\right] \tag{3.31}$$

Where AU is the astronomical unit and $r_{\odot}$ is the distance between the spacecraft and the Sun.

For what concerns the Propagator, the term in eq. (3.30), removed of the SRP term, is calculated in a similar fashion of the aerodynamic drag surface computations. In fact, the same in-house tool for dealing with satellite surface properties is used, which based on a 3D model of the spacecraft, generates lookup tables of the resulting force based on the incoming radiation direction.

Finally, the aspect of shadowing needs to be considered. In fact, in most of the LEO spacecrafts, configurations where the Earth occults partially or totally the Sun often occur. In these situations, the amount of sunlight which reaches the spacecraft is decreased or completely nullified. To model this effect, the shadow factor ν is introduced. This is a coefficient which can assume values between 0 and 1. If the spacecraft is in full sunlight, $\nu = 1$. If a total eclipse occurs and the Sun is completely occulted by the Earth, $\nu = 0$. When only a portion of the Sun disk is occulted by the Earth, the intermediate situation where ν is between 0 and 1 occurs. The way this parameter is modelled is analysed in the next section.

The complete SRP acceleration therefore becomes:

$$\ddot{\mathbf{r}}_{SRP} = -\nu P_{\odot} \frac{1AU^2}{r_{\odot}^2} \frac{A}{m} \cos(\theta_{\odot}) \left[(1-\epsilon)\mathbf{e}_{\odot} + 2\epsilon \cos(\theta_{\odot})\mathbf{n} \right] \tag{3.32}$$

3.4.1. Shadow Modelling

For what concerns the calculation of the shadow factor due to the presence of an occulting body in front of the Sun disk, an elementary, but quite common model, is the one of Montenbruck [17]. This formulation relies on geometry only, in the sense that only the superposition of the two surface disks of Earth and Sun is considered, neglecting any particular phenomenon, like the presence of the atmosphere, which could alter the result. In addition, perfectly spherical shapes are assumed for both bodies.

Within this model, some auxiliary coefficients are calculated as in eq. (3.33):

$$\begin{cases} a = \arcsin\left(\dfrac{R_{\odot}}{|\mathbf{r}_{\odot} - \mathbf{r}|}\right) \\ \\ b = \arcsin\left(\dfrac{R_B}{s}\right) \\ \\ c = \arccos\left(\dfrac{-\mathbf{s}^T(\mathbf{r}_{\odot} - \mathbf{r})}{s\,|\mathbf{r}_{\odot} - \mathbf{r}|}\right) \end{cases} \tag{3.33}$$

Where $R_{\odot}$ is the Sun radius, $\mathbf{r}_{\odot}$ is the distance between the spacecraft and the Sun, R_B is the radius of the occulting body, and $\mathbf{s}$ is the position vector of the spacecraft with respect to the occulting body (in case the occulting body is the Earth, $\mathbf{s} = \mathbf{r}$).

These three parameters are respectively the apparent radius of the occulted body (i.e. the Sun), the apparent radius of the occulting body, and the apparent separation of the centers of both bodies.

If the following condition is satisfied:

$$|a - b| < c < a + b \tag{3.34}$$

Then the area of the occulted segment of the apparent solar disk can be calculated as in eq. (3.35):

$$A = a^2 \cdot \arccos\left(\frac{x}{a}\right) + b^2 \cdot \arccos\left(\frac{(c-x)}{b}\right) - c \cdot y \tag{3.35}$$

Where:

$$\begin{cases} x = \dfrac{c^2 + a^2 - b^2}{2c} \\ \\ y = \sqrt{a^2 - x^2} \end{cases} \tag{3.36}$$

Finally, the shadow factor can be computed, as the remaining fraction of Sun light is given by eq. (3.37):

$$\nu = 1 - \frac{A}{\pi a^2} \tag{3.37}$$

If the condition in eq. (3.34) is not satisfied, additional cases can occur:

- $a + b \leqslant c$, no occultation takes place and the spacecraft is in full sunlight;
- $c < b - a$ implying that $a < b$, the occultation is total and no sunlight reaches the spacecraft;
- $c < a - b$ implying that $a > b$, the occultation is partial but maximum (annular eclipse).

As said, even though this model allows to compute the shadow factor also in intermediate shadow situations as the penumbra, it lacks some more advanced physical modelling when the Earth is considered as the occulting body. In this sense, when compared to more realistic models, the cylindrical model above described saw a penumbra time which was lower by more than a factor 2 [35].

For this reason, in addition to the conical shadow model, the more realistic SOLAARS-CF model by Robertson has been also included within PrOP. In this formulation, atmospheric effects due to solar radiation passing through the troposphere and stratosphere are modeled [25]. In addition, the oblateness of the shape of the Earth is taken into account. These highly physical shadow representations allowed to better model SRP accelerations when reproducing past LEO mission scenarios [35].

3.5. Earth Radiation Pressure

Analogously to the case of the Sun, also the radiation coming from the Earth generates a pressure on the spacecraft surfaces, the Earth Radiation Pressure (ERP). In this case two main components are distinguished: the shortwave optical radiation and the longwave

infrared radiation. The optical albedo component is generated by the reflection and scattering of incident solar radiation on the Earth's surface. The parameter ruling this ERP component is the albedo factor a, which has a global average value of 0.34 [17]. This component is only emitted by the daylight part of the Earth's surface. The infrared component is instead a near isotropic re-emission of the direct solar radiation absorbed by the Earth. The ruling parameter in this case is the emissivity e, with an average value of 0.68. However, this component is typically lower than the albedo. Both of these two effects decrease slightly with increasing altitude, therefore ERP accelerations will be higher for LEO satellites.

Despite being generated by the same physical principle of SRP, and therefore being a non-conservative force too, the numerical modelling of ERP perturbation can become more complex and delicate. This is due to the fact that in this case the illuminating object can no longer be assumed to be a point source. In fact, to account for the global ERP contribution of the whole Earth's surface portion viewed from the satellite, an integration over the whole spacecraft Field of View needs to be carried out. This is typically handled in ERP mathematical models by discretizing the Earth's surface into a certain number of elements, whose single contributions will then be accumulated to obtain the global effect [35]. In this regard, one of the earliest models, the one proposed by Knocke, is still a well-established standard [17], and therefore was implemented in the Propagator architecture.

This model assumes a diffuse Earth model. In fact, the portion of the Earth's surface which is visible to the satellite is divided in discrete segments. The radiation from each segment is calculated using Lambert's law of diffuse radiation, assuming that each segment may be approximated as a plane surface tangent to the center of the segment. This particular model divides the visible surface in a central cap and two outer rings, which are again discretized in 6 and 12 segments which have the same projected area of the central cap, therefore reaching a number of 19 elements with equal projected area [12]. However, more recent models have assumed finer discretizations.

The acceleration generated by this perturbation is calculated as in eq. (3.38):

$$\ddot{\mathbf{r}}_{ERP} = \sum_{i=1}^{N} C_R P_\odot \left(\tau a \cos(\theta) + \frac{e}{4}\right) \frac{A}{m} dA \mathbf{e}_j \tag{3.38}$$

Where N is the number of surface elements, C_R is the reflection coefficient, defined as $C_R = 1 + \epsilon$, $P_\odot$ is the Solar Radiation Pressure value at the Earth distance, τ is an eclipse factor which discriminates between surface segments in sunlight and shadowed ones, a, e

are the albedo and emissivity coefficients respectively, θ is the angle between the surface element normal vector and the Sun direction, dA is the projected area of the single surface element. This last parameter can be computed using the case of the central cap, which will provide for the projected area of each segment, as follows.

First of all, the angular limit of the surface visible from the satellite is computed:

$$\zeta_M = \arcsin\left(\frac{R_\oplus}{r}\right) \tag{3.39}$$

Then, the angular limit of the central cap can be evaluated:

$$\zeta_1 = \arccos\left(\frac{N - 1 + \cos(\zeta_M)}{N}\right) \tag{3.40}$$

From which the projected area computation follows:

$$dA = 2(1 - \cos(\zeta_1)) \tag{3.41}$$

For the complete geometrical formulation for the calculation of the geometrical properties of each surface segment, the reader is referred to the original work of Knocke [12].

For what concerns the albedo and emissivity coefficients, in the original model they were calculated using simple spherical harmonic expansions truncated at the second order [12]. These were obtained by fitting available data collected at the time of formulation. However, more recent models are based on actual Earth radiation measurements collected on top of the atmosphere in the framework of the Clouds and Earth's Radiant Energy System (CERES) [35]. At the present state of development of the Propagator, only the first option is available, but the inclusion of this externalized source of data is being considered for further updates.

As for the SRP, also in this case the cross section area of the satellite A, seen by the rays coming from each surface element, is calculated using the in-house surface modelling tool.

3.6. Relativistic Correction

Taking into consideration the accuracy demand of the discussed Propagator, the effects derived from the theory of General Relativity can no longer be neglected [27]. In fact, due to the fact that the Earth, given its mass and angular momentum, leads to a curvature

of the four-dimensional space-time, the Earth-orbiting spacecrafts experience a motion which no longer completely respects the classical Newton theory of gravitation. However, given that the masses of artificial satellites are negligible with respect to the mass of the central body, the velocities of such satellites are much smaller than the speed of light, and considering that the size of the Earth, as the one of the satellite's orbits, are much larger than the Earth's Schwarzschild radius, the effects of the General Relativity on the spacecraft orbits can be simplified by means of the so called Post-Newtonian approximation [30]. This results in an additional acceleration term to be included in the equations of motion, just as for classical perturbations.

The mathematical formulation of this relativistic correction suggested by the IERS Conventions for Earth-orbiting satellites [22], expressed in a geocentric inertial frame, is reported in eq. (3.42):

$$\begin{aligned}\ddot{\mathbf{r}}_r =& \frac{GM}{c^2 r^3}\left(\left(4\frac{GM}{r} - v^2\right)\mathbf{r} + 4\left(\mathbf{r}\cdot\mathbf{v}\right)\mathbf{v}\right) + 2\left(\boldsymbol{\Omega}\times\mathbf{v}\right) \\ &+ 2\frac{GM}{c^2 r^3}\left(\frac{3}{r^2}\left(\mathbf{r}\times\mathbf{v}\right)\left(\mathbf{r}\cdot\mathbf{J}\right) + \left(\mathbf{v}\times\mathbf{J}\right)\right)\end{aligned} \tag{3.42}$$

With

$$\boldsymbol{\Omega} = \frac{3}{2}\mathbf{v}_{B/S}\times\left(-\frac{GM\mathbf{r}_{B/S}}{c^2 r_{B/S}^3}\right) \tag{3.43}$$

$$\mathbf{J} = \mathbf{R}_B^{I/F}\begin{bmatrix}0 & 0 & \frac{2}{5}R_B^2\omega_b\end{bmatrix} \tag{3.44}$$

$\mathbf{r}_{B/S}$ and $\mathbf{v}_{B/S}$ are the position and velocity of the Earth with respect to the Sun, $\mathbf{J}$ is the Earth's angular momentum per unit mass, $\mathbf{R}_B^{I/F}$ is the Earth fixed to inertial frame rotation matrix, R_B is the Earth's radius and ω_b is the Earth's spin rate.

In eq. (3.42), the first term is the Schwarzschild term, the second one is the geodetic precession (or de Sitter precession) and the third one is the frame-dragging effect (or Lense-Thirring effect). Other relativistic effects could be included in the formulation, mainly due to the presence of other celestial bodies, but due to their very small magnitudes they are often neglected [9].

The Schwarzschild term is the biggest among the three, and all of them show both secular and periodic effects on the orbit geometry.

3.7. Orbit Control Maneuvers

To counteract the perturbations already described, or in general to keep or modify their orbit parameters, satellites are often equipped with thrusters used for Orbit Control Maneuvers. Of course, these introduce additional accelerations which are needed to be taken into account during the propagation. However, differently from the perturbations, control maneuvers consume the onboard propellant. This causes a change of mass which needs to be considered during the propagation, as it is a fundamental parameter for the computation of non-conservative accelerations.

For these reasons, the Propagator was equipped with the possibility of dealing with continuous control maneuvers provided in the input configuration file. In this regard, two possible alternatives can be chosen:

- Linear Control Maneuver: maneuvers with constant thrust and mass flow rate, therefore causing a linear variation of the spacecraft mass, hence the name. In this case several parameters combination can be provided as input, e.g. thrust and duration, or total Δv and specific impulse;
- File-Based Maneuver: in this case an external CSV file is provided, with general time profiles of thrust and mass flow rate. This is the most general option.

Whatever the input, the resulting maneuver acceleration at a specific time instant is always computed as the ratio between thrust and mass at that time. This means that, in case of Linear maneuver, there might be input parameters combinations which require analytical treatment to obtain an explicit thrust value, if not explicitly provided in the configuration file.

For instance, in case the Δv, mass flow rate $\dot{m}$ and maneuver duration Δt are provided, the thrust $\mathbf{T}$ can be obtained as in eq. (3.45):

$$\mathbf{T} = \frac{|\dot{m}|}{-\ln\left(1 - \dfrac{|\dot{m}|\Delta t}{m_0}\right)}\mathbf{\Delta v} \tag{3.45}$$

The input thrust or $\mathbf{\Delta v}$ vectors are usually provided in the spacecraft body frame or in the RTN frame, therefore appropriate frame transformation, which might require attitude information, is needed before propagation.

An important aspect of dealing with Orbit Control Maneuvers, is that they introduce discontinuities in the numerical integration. This issue will be analysed in detail in chapter 4,

along with the techniques implemented to tackle it.

4 | Numerical Integration

As stated in chapter 2, numerical integration of the equations of motion is the only method capable of reaching the level of accuracy demanded for PrOP, given all the perturbations which are needed to be taken into account.

Again, the core of this technique is to numerically solve first order differential equations of the form of eq. (2.1), which can always be recovered through appropriate manipulation from the original equations of motion. This solutions is recovered by using particular algorithms, which take the name of numerical integrators. A variety of these has been studied and developed for decades, and many of them have found successful application in the field of astrodynamics [17].

However, there also exist other ways to formulate the ODE to numerically integrate, apart from the Cowell one reported in eq. (3.3), such as the Encke's formulation, which was also implemented in the software.

Finally, in chapter 2 it was stated that modifying the floating point precision for the numerical representation of some numerical components could lead to a better overall result, which was confirmed by some case studies. This modification also acts on the numerical processes of the Propagator and is therefore reported in this chapter.

Therefore, hereafter, the solutions implemented in the Propagator are summarised. For an in-depth description of some of these components, the reader is suggested to refer also to the previous reported works about this software [31].

4.1. Numerical Integrators

Numerical integrators usually discretize the time domain into a certain number of steps, and then proceed to calculate progressively the solution function at each discretized time instant, by using recursively eq. (4.1):

$$\mathbf{y}(t_n + h) = \mathbf{y}(t_n) + \int_{t_n}^{t_n+h} \mathbf{f}(t, \mathbf{y}(t))dt \tag{4.1}$$

Where $\mathbf{y}(t)$ is the solution of the equation (i.e. the spacecraft state), h is the stepsize (i.e. the Δt), and $\mathbf{f}(t, \mathbf{y}(t))$ is the function to integrate (i.e. the velocities and accelerations).

This is done by approximating in a certain way, which differs with the algorithms, the integral term, as analytical integration is in most of the cases not possible.

As previously stated, a wide variety of integrators are available nowadays for solving even very complex ODEs, thanks to the great number of possible applications fields and of the exponential increase in computational power of the modern personal computers. On the other hand, due to this vastness of solutions, it is difficult to univocally identify a technique which is best for a specific application and most of all, sufficient for a variety of input configurations.

In fact, the cathegories in which numerical integrators are grouped often provide different benefits:

- Singlestep methods are very easy to implement, can be applied to a high number of problems and the stepsize can be easily manipulated for error control;
- Multistep methods are characterised by a high efficiency;
- Extrapolation methods offer a high accuracy.

Therefore, a tradeoff in the impementations needed to be carried out to guarantee requirements meeting in all possible conditions. This led to the inclusion of several singlestep and multistep integrators in the software, described in the following sections.

4.1.1. Single-step integrators

Singlestep integrators use only support points belonging to the time interval which is being integrated. For this reason, modifications of the stepsize do not require much computational effort as it can be done while maintaining previously calculated points. The most common class of singlestep integrators is the one of the Runge-Kutta methods.

By assuming the notation for which $\mathbf{y}(t_n + h) = \mathbf{y}_{n+1}$ and $\mathbf{y}(t_n) = \mathbf{y}_n$, the general Runge-Kutta formula for step advancement can be written as in eq. (4.2):

$$\mathbf{y}_{n+1} = \mathbf{y}_n + h \sum_{i=1}^{M} b_i \mathbf{k}_i \tag{4.2}$$

With:

$$\begin{cases} \mathbf{k}_1 = \mathbf{f}(t_n + c_1 h, \mathbf{y}_n) \\ \\ \mathbf{k}_i = \mathbf{f}(t_n + c_i h, \mathbf{y}_n + h \sum_{j=1}^{i-1} a_{ij} \mathbf{k}_j) \quad (i = 2, ..., M) \end{cases} \tag{4.3}$$

Where h is the stepsize, M is the number of stages of the integrator, a, b, c are constant coefficients peculiar of the Runge-Kutta scheme in use. In other words, each of these methods is fully described by a set of coefficients, which obey to some relationships and are usually provided in tables called Butcher arrays.

A method which is capable of approximating the solution up to terms of order h^p is called a pth-order method, and it is therefore a figure of merit for determining the truncation error of that particular integrator. To reduce this error, either higher-order integrators can be used, or finer stepsizes. For low order Runge-Kutta integrators, it is found that the order is equal to the number of stages, but this is not anymore true for higher order schemes [17].

Since the magnitude of the variation in time of the function to integrate (i.e. the derivative of the solution) can vary also greatly with time, as in the case of highly elliptical orbits, if the stepsize is kept fixed then the integration error could rapidly increase. To manage this, stepsize control can be implemented to ensure an almost constant error, even when the solution rapidly evolves.

To do this, first of all the error needs to be estimated. The most common way to do that within Runge-Kutta methods is to integrate the same step with two different schemes, one of order p and one of order $p+1$ with the same stepsize h, obtaining the solutions $\mathbf{y}_{n+1}$ and $\hat{\mathbf{y}}_{n+1}$, respectively. One would be led to use the higher order solution for error estimation, while then considering the lower order solution as the final output of the integration, but Dormand and Prince showed that the opposite is also true, and leads to the advantage of having a final solution of higher order with the same amount of stages [31]. The error is then calculated as in eq. (4.4):

$$e = |\hat{\mathbf{y}}_{n+1} - \mathbf{y}_{n+1}| \tag{4.4}$$

The commonly used technique for stepsize control assumes a certain maximum tolerance T for the error. In this way, the corrected stepsize h^* can be calculated as in eq. (4.5):

$$h^* = 0.9h \left(\frac{T}{e} \right)^{\frac{1}{M+1}} \tag{4.5}$$

In addition, in order to avoid rapid oscillations of the stepsize, it is suggested to limit the possible variation of the stepsize to a factor 2 - 5 [17]. For this reason, the final check is carried out:

$$h^* = \min(h^*, 5h) \tag{4.6}$$

To avoid doubling the computational cost of stepsize control by using two completely separate integrators, embedded Runge-Kutta methods are used. These are a category of neighbouring order integrators which share the same a and c coefficients, and only differ by the b coefficients. In this way, the two methods will have the same $\mathbf{k}_i$ values, and can easily be used for stepsize control.

An alternative Runge-Kutta formulation also exists to directly integrate second order differential equations. It is the case of the Runge-Kutta-Nyström method. This class of integrators shows advantages with respect to classical Runge-Kutta methods when the function to integrate does not depend on the first derivative of the state. In orbital propagation, this would mean that Runge-Kutta-Nyström could be more efficient for orbits in which the acceleration does not depend on the velocity. However, since this is not true for several perturbations reported in chapter 3, this class of algorithms is not analysed further.

To sum up, Runge-Kutta integrators are easy to implement and can easily include stepsize control for error mitigation. However, they tend to be less efficient, especially in the case of higher order methods, than other algorithms, due to the high number of function evaluations required for each step.

4.1.2. Multi-step integrators

One of the drawbacks of the singlestep methods is that every time that there is a progression in the integration, the values calculated for the previous steps are discarded and no longer used in the next step. In the case of high order integrators (i.e. integrators with a high number of stages) and/or with quite complex functions which require many arithmetical operations to be evaluated, this could increase dramatically the computational time.

To avoid this, there exists another class of numerical integrators, which store previously calculated points to use them also in successive integration steps, in order to limit the number of function evaluations for each step progression. For this reason, they are called multistep integrators.

The main principle for these integrators is that, if integrating from t_n to $t_n + h$, as in eq. (4.1), the function $\mathbf{f}$ to integrate is approximated by a polynomial of order $M - 1$, obtained with the interpolation of M previously calculated points. The polynomial can be obtained via the Newton's formula for a polynomial p^M of order $M - 1$, which leads to Adams-Bashforth method:

$$\mathbf{y}_{n+1} = \mathbf{y}_n + \int_{t_n}^{t_{n+1}} p_n^M(t)dt = \mathbf{y}_n + h \sum_{j=0}^{M-1} \gamma_j \nabla^j \mathbf{f}_n \tag{4.7}$$

Which makes use of the backward difference operator ∇^j of the i-th function evaluation $\mathbf{f}_i$, which is defined recursively as in 4.8:

$$\begin{aligned} \nabla^0 \mathbf{f}_i &= \mathbf{f}_i \\ \nabla \mathbf{f}_i &= \mathbf{f}_i - \mathbf{f}_{i-1} \\ \nabla^n \mathbf{f}_i &= \nabla^{n-1} \mathbf{f}_i - \nabla^{n-1} \mathbf{f}_{i-1} \end{aligned} \tag{4.8}$$

Where the stepsize independent coefficients can be obtained recursively using:

$$\gamma_j = 1 - \sum_{k=0}^{j-1} \frac{1}{j+1-k} \gamma_k \tag{4.9}$$

However, by substituting the definitions of the backward differences in eq. (4.7), an explicit relationship between the next step and the previous function evaluations can be obtained.

A problem of this method is based on the fact that we are assuming that the constructed polynomial remains valid also between t_n and t_{n+1}, which in general is only an approximation. To solve this problem, the Adams-Moulton method uses the M points between t_{n-M+2} and t_{n+1} to approximate the polynomial to integrate. However, this leads to an implicit formulation as the function evaluation at t_{n+1} is required in this case, but this is not known a-priori, therefore an iterative procedure is required.

One way to handle this issue is with the so called Predictor-Corrector or Predict-Evaluate-Correct-Evaluate (PECE) algorithms. It is the case of the Adams-Bashforth-Moulton

method, which uses an explicit Adams-Bashforth method to calculate the first evaluation of the function at t_{n+1}, which is then used as initial value in an iterative procedure to reach convergence using instead the Adams-Moulton method repeatedly.

As for the singlestep methods, also in the case of multistep integrators a formulation which aims to solve directly a second order differential equation can be reached, it is the case of the Stoermer-Cowell methods. In fact, by assuming that the function is again not dependent on the state first derivative, the following Stoermer predictor is obtained:

$$\mathbf{y}_{n+1} = 2\mathbf{y}_n - h\mathbf{y}_{n-1} + h^2 \sum_{j=0}^{M-1} \delta_j \nabla^j \mathbf{f}_n \tag{4.10}$$

An implicit Cowell corrector can then be applied:

$$\mathbf{y}_{n+1} = 2\mathbf{y}_n - h\mathbf{y}_{n-1} + h^2 \sum_{j=0}^{M-1} \delta_j^* \nabla^j \mathbf{f}_{n+1} \tag{4.11}$$

Here the coefficients of the Stoermer-Cowell method δ_j and δ_j^* can be analytically obtained from the ones of the implicit Adams method.

However, due to the assumption of no dependence from the first derivative, these formulation can again lead to errors in case of acceleration which depends on the velocity. This can be solved by using two different predictors and correctors combinations for the calculation of the next full state. In fact, by using as Stoermer and Adams-Bashforth respectively for state and state derivative predictors, jointly with Cowell and Adams-Moulton respectively as correctors, the Adams-Cowell formulation is reached.

Finally, the Gauss-Jackson or second sum methods are introduced. These are slightly modified versions of the Stoermer-Cowell methods, and probably the most recommendable fixed-stepsize multistep methods for orbit computations [17]. The computations of these algorithms involve the use of first and second sums, which are a generalized version of the backward differences:

$$\begin{aligned} \mathbf{f}_i &= \nabla^{-1}\mathbf{f}_i - \nabla^{-1}\mathbf{f}_{i-1} \\ \nabla^{-1}\mathbf{f}_i &= \nabla^{-2}\mathbf{f}_i - \nabla^{-2}\mathbf{f}_{i-1} \end{aligned} \tag{4.12}$$

For solving this implicit relations, an initial guess for the first and second sums need to be provided, after which an iterative procedure can lead to the converged solution.

4.1.3. Discontinuity control

As already mentioned in chapter 3, some force models, as the thrust, introduce numerical discontinuities in the propagation. For example, this happens when a thruster is turned on or off. In this case, a discontinuous acceleration is included in total acceleration to integrate, which can cause several numerical problems.

To understand this issue, a sample case in which an orbit control maneuver starts at a generic propagation time, which is different from the time points contained in the discretized timegrid, is reported in fig. 4.1:

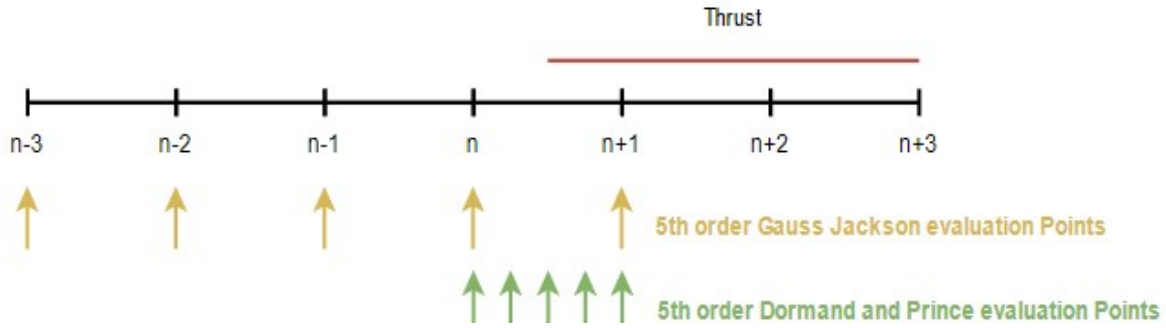

Figure 4.1: Discontinuity introduced by Orbit Control Maneuver

Looking at the picture, two main issues can be brought up:

- Part of the acceleration (and so part of the total ΔV) is not considered due to the finite number of function evaluations. This is particularly evident in the case of the multistep case, and leads to errors in the maneuver ΔV reconstruction. In addition, if the maneuver is too short or the stepsize too large, the maneuver could even be entirely missed;
- Considering that the high order integrators use several support points for the step progression, it might happen that some intermediate points of the step will evaluate a nonzero thrust, while others of the same step will evaluate a zero thrust. This difference of evaluations in the same step can lead to numerical instability, as it contradicts the continuity assumption of the underlying function to integrate.

For these reasons, some sort of discontinuity control needed to be implemented to avoid a drastic increase in the integration error in the case of orbit control maneuvers.

The process, managed by the integrators, which was implemented as a solution for this problem, is represented in fig. 4.2.

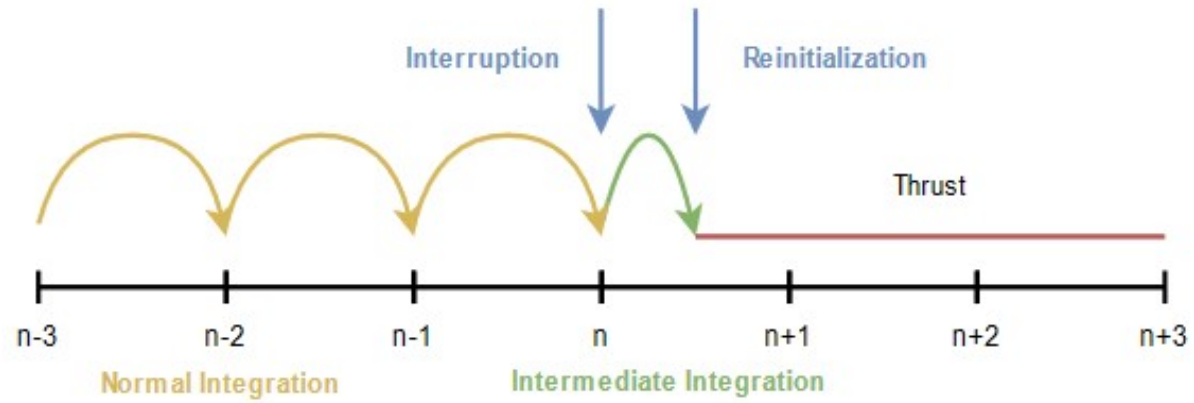

Figure 4.2: Discontinuity Control Process

The operations carried out by the integrators are schematized as follows:

1. Assuming no discontinuities were found in past integration steps, the integrator is carrying out the "normal integration". At the start of each new step a detection process is activated, in order to find if new discontinuities are introduced in the selected timestep. This is possible as the input maneuver history is already known at the start of the propagation;

2. If a discontinuity is found to occur in the timestep of interest, the normal integration is interrupted. In addition, the Δt and the time at which the discontinuity occurs are stored in the integrator. In case multiple discontinuities are present in the same step, the earliest one will be stored;

3. The Δt of the current step is then modified in order to "reach" the discontinuity with the next integration step. For instance, if a discontinuity is present at time t^* in the step from t_n to t_{n+1}, the new stepsize will be set to $\Delta t = t^* - t_n$. The step is finally calculated, in this intermediate integration;

4. Following the intermediate integration, a new discontinuity detection is carried out. If a new discontinuity will happen in the next step, the integration is again interrupted, and the intermediate integration will happen again, until no new discontinuities are found. In this case, the integrator is reinitialized, meaning that the original stepsize is restored, and the normal integration can begin again.

However, some final remarks need to be reported. In fact, if for singlestep integrators no major issues rise up thanks to their independence between the steps, multistep integrators on the other hand are less prone to changes in the stepsize. In fact, as stated previously, multistep integrators require a certain number M of equally spaced previously calculated

support points to progress in the integration. In the discontinuity control process reported above, there is a forced change in the stepsize, meaning that the previously stored values can no longer be used for progressing as the assumption of spacing uniformity is not true anymore.

For this reason, in PrOP multistep integrators were designed in such a way that, if a discontinuity is detected and therefore old evaluation points are invalidated, the integration is carried out by an auxiliary singlestep integrator. Once this auxiliary integrator has collected the necessary number of equally spaced support points, the multistep integrator can be reinitialized and resume its normal integration procedure.

4.2. ODE Strategy

The equation of motion to integrate was already expressed in the classical Cowell formulation in eq. (3.3). However, a downside of this way to write the differential equation is that perturbing accelerations with very different orders of magnitude are summed at each timestep. This could lead to an increase in the roundoff error.

A formulation which aims to reduce this error is the Encke's method. Its underlying concept is that the central body gravity term dominates over the other accelerations, which in fact are only seen as perturbations. In other words, the main reference of the propagation result is the classic Kepler orbit, even though the complete solution will slightly drift away from this baseline as the propagation time increases. Due to this, instead of directly integrating the full state, one could think of integrating the deviation of the actual solution from the Kepler orbit.

Therefore, considering the two distinct accelerations of the central body gravity $\ddot{\mathbf{r}}_0$ and remaining perturbations $\ddot{\mathbf{r}}_{pert}$, such that:

$$\ddot{\mathbf{r}} = \ddot{\mathbf{r}}_0 + \ddot{\mathbf{r}}_{pert} \tag{4.13}$$

And writing the new state with the position and velocity deviations from the Kepler orbit $\boldsymbol{\xi}(t)$:

$$\begin{aligned} \Delta\mathbf{r}(t) &= \mathbf{r}(t) - \boldsymbol{\xi}(t) \\ \Delta\dot{\mathbf{r}}(t) &= \dot{\mathbf{r}}(t) - \dot{\boldsymbol{\xi}}(t) \end{aligned} \tag{4.14}$$

The new equation of motion to integrate becomes:

$$\begin{aligned} \frac{d\Delta\mathbf{r}}{dt} &= \Delta\dot{\mathbf{r}} \\ \frac{d\Delta\dot{\mathbf{r}}}{dt} &= \Delta\ddot{\mathbf{r}}_0 + \ddot{\mathbf{r}}_{pert} \end{aligned} \tag{4.15}$$

With:

$$\Delta\ddot{\mathbf{r}}_0 = \ddot{\mathbf{r}}_0 - \ddot{\boldsymbol{\xi}} \tag{4.16}$$

Both these terms indicate central gravity accelerations, referred to the actual and reference orbits, respectively. By making explicit this acceleration formulation, we obtain:

$$\Delta\ddot{\mathbf{r}}_0 = -GM\left(\frac{\mathbf{r}}{|\mathbf{r}|^3} - \frac{\boldsymbol{\xi}}{|\boldsymbol{\xi}|^3}\right) \tag{4.17}$$

Position and velocity can then be obtained from the state variables using eq. (4.14).

However, this formulation is based on the assumption that the deviation of the real orbit from the Kepler one is small. This will not be true for prolonged periods of propagation, so integration errors might occur.

This deviation from the reference solution is monitored through the Encke ratio, defined as:

$$\epsilon = \frac{|\Delta\mathbf{r}|}{|\mathbf{r}|} \tag{4.18}$$

The threshold value which guarantees a good propagation is not univocal, even though literature studies seem to agree that values between 1% and 10% most likely allow to meet satisfactory accuracies [31].

If during propagation this limit is passed, in order to keep the accuracy sufficiently high, a new reference orbit is needed, so the rectification is carried out. This process resets the reference with a new orbit having initial conditions equal to the propagation state at the time of rectification, every time the Encke ratio threshold is reached. However, this makes this procedure not suitable for multistep methods, as the rectification would need a re-initialization of the integrator.

For the choice of the reference orbit, the simplest solution would be to use a simple Keplerian orbit with initial conditions set equal to the initial state. However, more accurate

and complex references might be adopted, although this would increase the computational cost of the method [31].

4.3. Hybrid Precision

Another method which was used in the Propagator for the mitigation of the roundoff error was the implementation of Hybrid Precision. To understand this, it is important to recall the source of this error. In fact, it is caused by how floating point numbers are represented and stored with a finite number of digits. Due to this, the error accumulates everytime a mathematical operation is carried out with two or more variables, therefore for finer stepsizes, or in other words increasing the number of steps and therefore of operations to complete the integration, the roundoff error can exceed the prescribed limit.

Most modern software applications use single or double precision, so switching to the superior quadruple precision would ideally improve this error, as it would shift the wrong digits to the trailing edge of the stored variable. Nevertheless, the main issue about the usage of quadruple precision is the dramatic increase in the computational time which results from its implementation.

An intermediate way to exploit quadruple precision without jeopardizing the computational burden of the Propagator is the Hybrid Precision method, suggested by Nie [16]. This proposal suggests to implement the quadruple precision only in the integration part of the software, while keeping the force models formulation (i.e. the accelerations computation) in double precision. This comes from the fact that the complex force models, especially when used simultaneously, correspond to the main part of the computational time. Despite this, part of the integration error comes from the integration operations.

The implementation of the Hybrid Precision, following the results reported by Nie, proved well also for PrOP, as already shown in chapter 2. In fact, it allowed to reach and even surpass the accuracy requirement of the Propagator, whith only a small percentage increase in computational time. Furthermore, this increase becomes almost negligible when a higher number of force models is used for the propagation.

5 | Analysis and results

In chapter 2, the main results of the past investigations involving the numerical aspects of the Propagator were reported. These highlighted that the accuracy requirement could be satisfied when using certain high order integrators, together with the Hybrid Precision, meaning that the truncation and roundoff errors coming from the integration were successfully minimised. However, in order to obtain a realistic orbit for the POD purposes mentioned in chapter 1, knowledge about the effect that every force model has on the propagation results is needed, in order to understand to which extent model the dynamics of the spacecraft and to be able to critically analyse such results.

To achieve this, a series of analyses involving the dynamical models implemented for this Master Thesis were carried out. First of all, the single accelerations and displacement caused by every force model were computed along four input orbits, chosen to represent four different orbital classes to better grasp how these perturbations act on different orbit configurations. Furthermore, several sensitivity analyses were executed for particular force models aspects and configurations, jointly with a brief report on the computational cost introduced by each perturbation. Then, the effect of the implementation of the Discontinuity Control in the integrators was studied. Finally some validation tests to compare the Propagator results with STK were run.

5.1. Acceleration and Displacement Analysis

In order to understand the magnitude of the effects coming from each single perturbation, the acceleration is the first figure of merit which comes to mind. Furthermore, given the formulation of the Reduced-Dynamic POD techniques, which still represent the main framework of this Propagator, acceleration values are extremely important for what concerns the state estimation, and the calibration of the empirical accelerations which have to be provided during the propagation. Therefore these were the first values computed for the Force Models analyses.

Nevertheless, for more general flight dynamics applications, the mapping between accel-

eration values and actual physical effects on the orbit is often not trivial. This partially happens due to the fact that, as we will see, accelerations with similar orders of magnitude but with other different parameters, as direction or time variation, can cause very distinguished deviations on the orbits. To quantify this deviation, together with the accelerations, also the displacements with respect to a nominal Kepler orbit, obtained propagating with the central gravity and the analysed perturbation only, were computed and reported. In this way, a slightly more "physical" influence of the different dynamical models on the orbit was shown, which could be useful for a wider variety of uses of the software.

In order to cover different orbital regimes and therefore characterise also how perturbations have different effects depending on orbit geometry, the initial state vectors for each simulation were selected from the orbital elements reported in table 5.1. This was to follow the approach of past analyses studies [34], where orbits from LEO to GEO were considered.

	Name	a **(km)**	e	i **(deg)**	Ω **(deg)**	ω **(deg)**	θ **(deg)**
LEO	TerraSAR-X	6886	0.00018	97.45	295.85	80.81	340.08
MEO	NAVSTAR 50 GPS	26560	0.00370	55.24	82.21	191.50	215.96
HEO	Molniya 3	10115	0.57873	63.22	354.69	311.23	11.72
GEO	Galaxy 11	42165	0.00007	0.03	123.00	45.00	87.00

Table 5.1: Keplerian Elements of Input Orbits

A 3D visualisation of such orbits is also reported in fig. 5.1. It must be noted that these input orbits choice shall not be considered exhaustive, even though it allowed to highlight some rough trend.

Again, following the choice of past analyses, the initial propagation epoch, January 4 2003, was chosen in order to run the simulations in a period of medium solar activity. Another important reason to choose dates enough in the past was to guarantee the completeness and reliability on space weather and Earth Orientation Parameters (EOP) measurements [34].

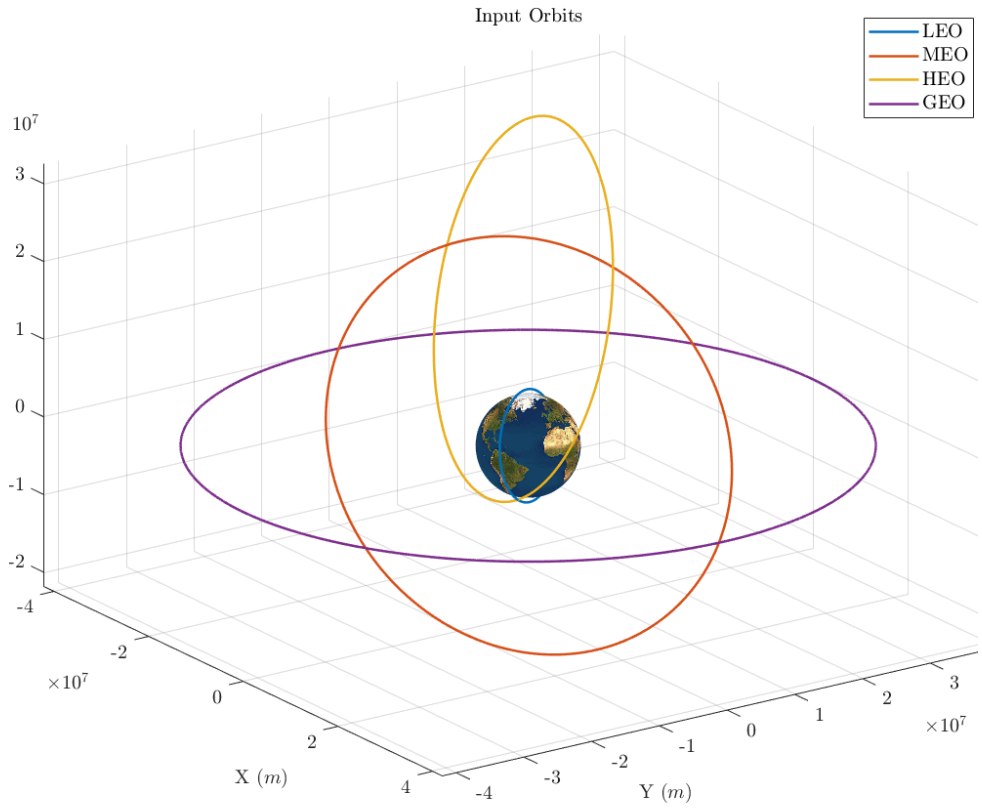

Figure 5.1: Input Orbits 3D Visualization

For what concerns the modelling of the satellite surfaces, which is used when computing non-conservative forces, in order to construct a realistic scenario, the 3D model of the TerraSAR-X satellite, an artistic illustration of which is reported in fig. 5.2, was used.

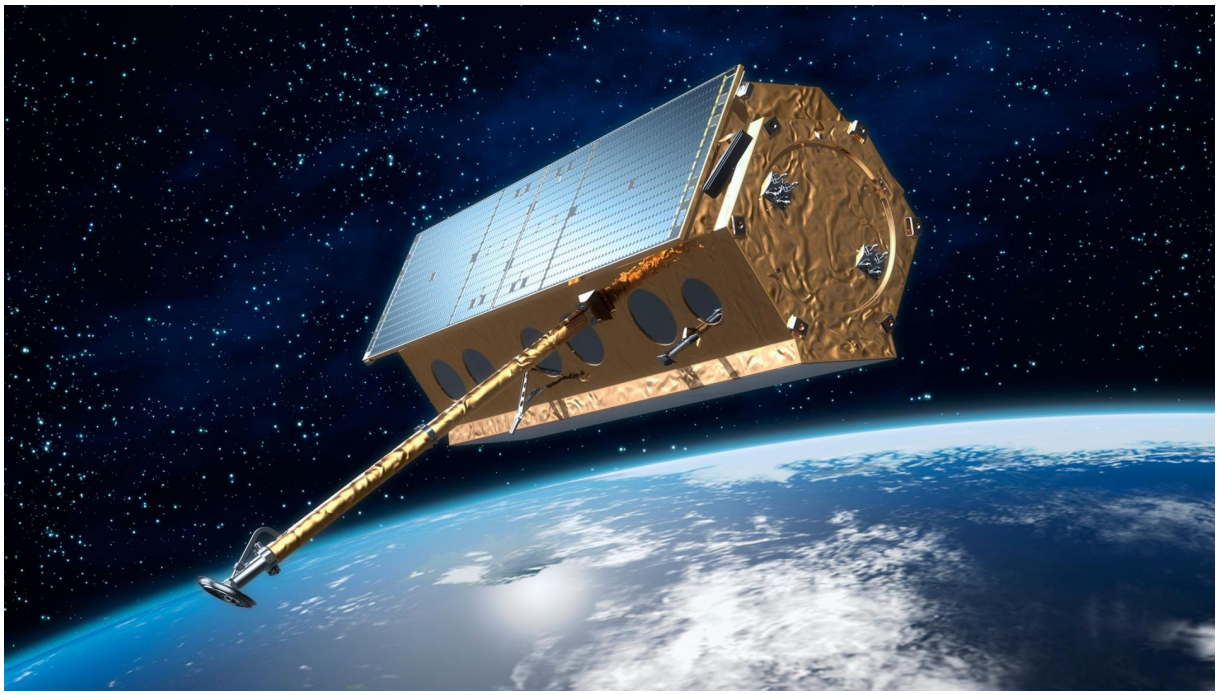

Figure 5.2: TerraSAR-X (Credits: EADS Astrium)

It has to be noted that its shape is quite peculiar, and offers an area to mass ratio of less than 10^{-3} m^2/kg in the along track direction, which is quite a low value. As a result, the effect of aerodynamic drag could be seen as slightly underestimated when compared to other spacecrafts with significantly larger ratios.

The effects (both accelerations and displacements) of the employed force models acting on the LEO orbit for a 24 hours propagation are reported in fig. 5.3. The gravitational accelerations (central gravity, geopotential and third body) are the highest ones, whereas for the non-conservative forces drag has the maximum values, even though SRP and ERP differ by less than one order of magnitude. This can be explained as said by the low area to mass ratio of the spacecraft model. For what concerns the SRP accelerations, the eclipse periods are quite visible. It is interesting to notice that also the ERP follows a periodic pattern due to the eclipse. This is caused by the fact that, on the dark side of the Earth, the albedo component is absent. Relativity is the lowest acceleration, with values in the orders of tenth of nm/s^2.

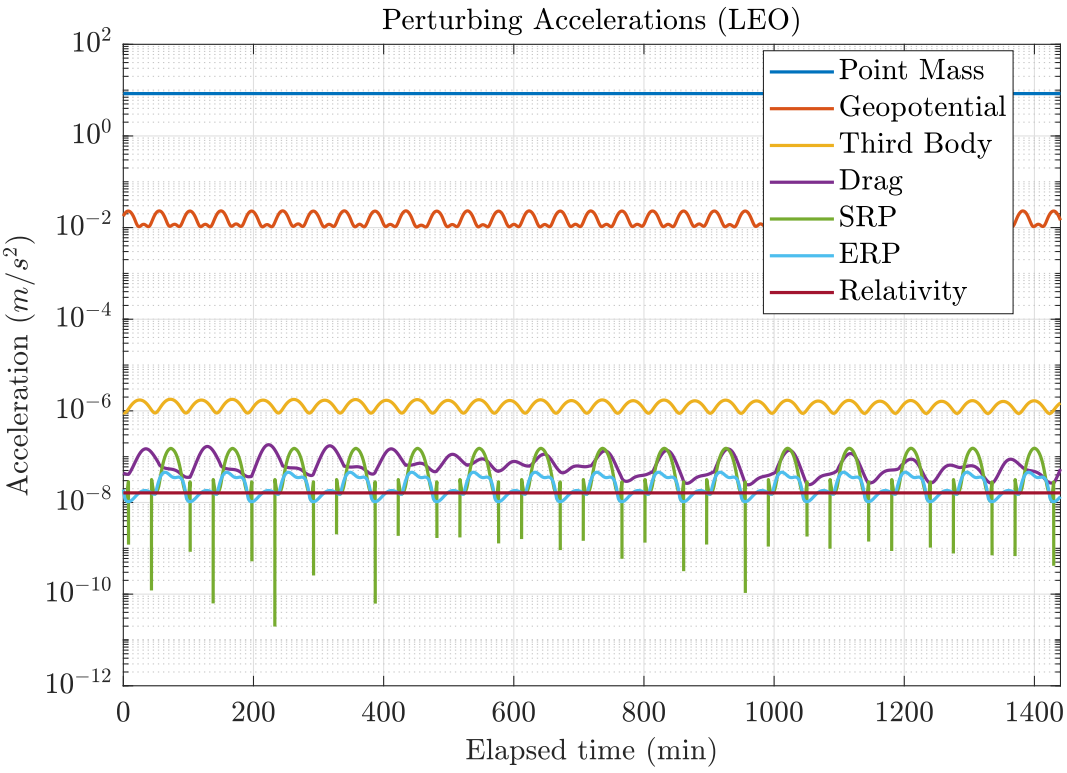

(a) Accelerations

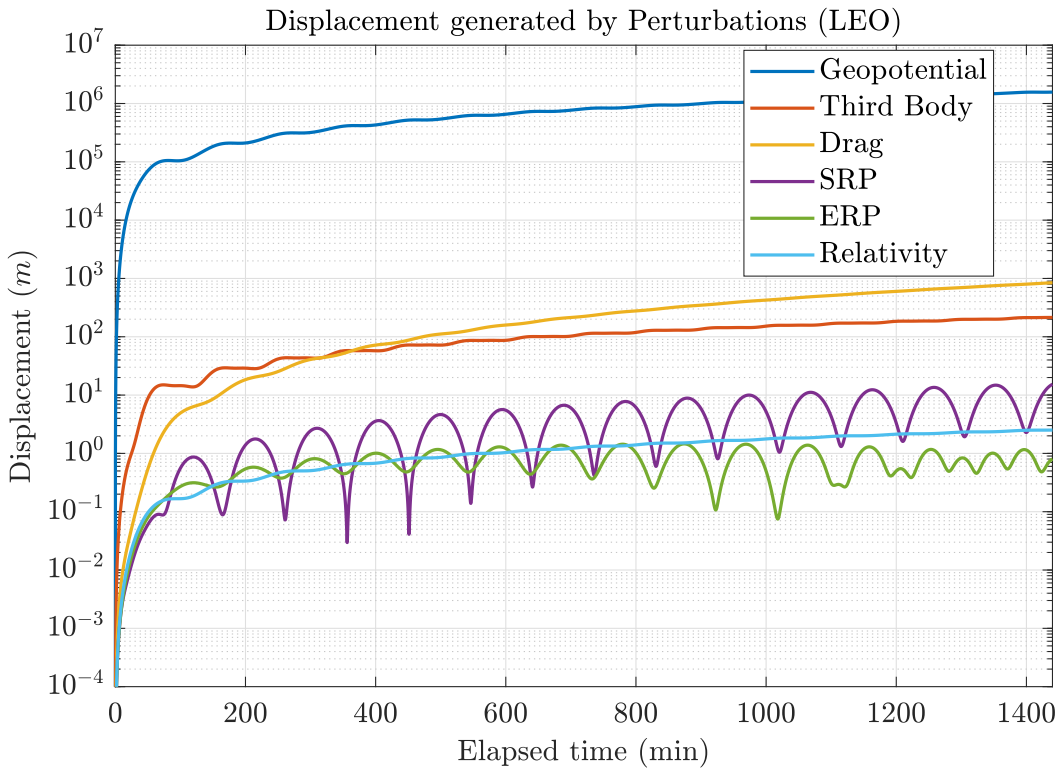

(b) Displacements

Figure 5.3: Perturbation Effects in LEO

The displacement analyses provides very similar results. Geopotential and third body cause deviations from the nominal orbit of 1000 km and 100 m, respectively. Interestingly, drag produces higher displacement than the luni-solar perturbation, reaching km-level displacements. SRP and ERP show some signs of the eclipses also in this case, reaching meter and sub-meter level of displacements. Relativity, probably due to its quite constant value, even surpasses the displacement caused by the albedo, reaching meter level deviations.

In terms of force models hierarchy, the MEO analysis, depicted in fig. 5.4, shows no big variations. It must be noted that at the GPS altitude, drag is already negligible in practice, due to the almost null atmospheric density. The effects of the Earth gravity field are definitely lower due to the increased altitude, as ERP and Relativity accelerations. On the contrary, SRP acceleration shows higher peaks, together with limited eclipse time compared to the LEO case. Also the third body accelerations increases by almost two orders of magnitude thanks to the greater semi-major axis.

The displacement effect pattern is quite similar. Interestingly, in the MEO case geopotential and third body perturbations cause comparable deviations, in the order of km. The SRP is the dominating non-gravitational effect, with displacement of hundreds of meters.

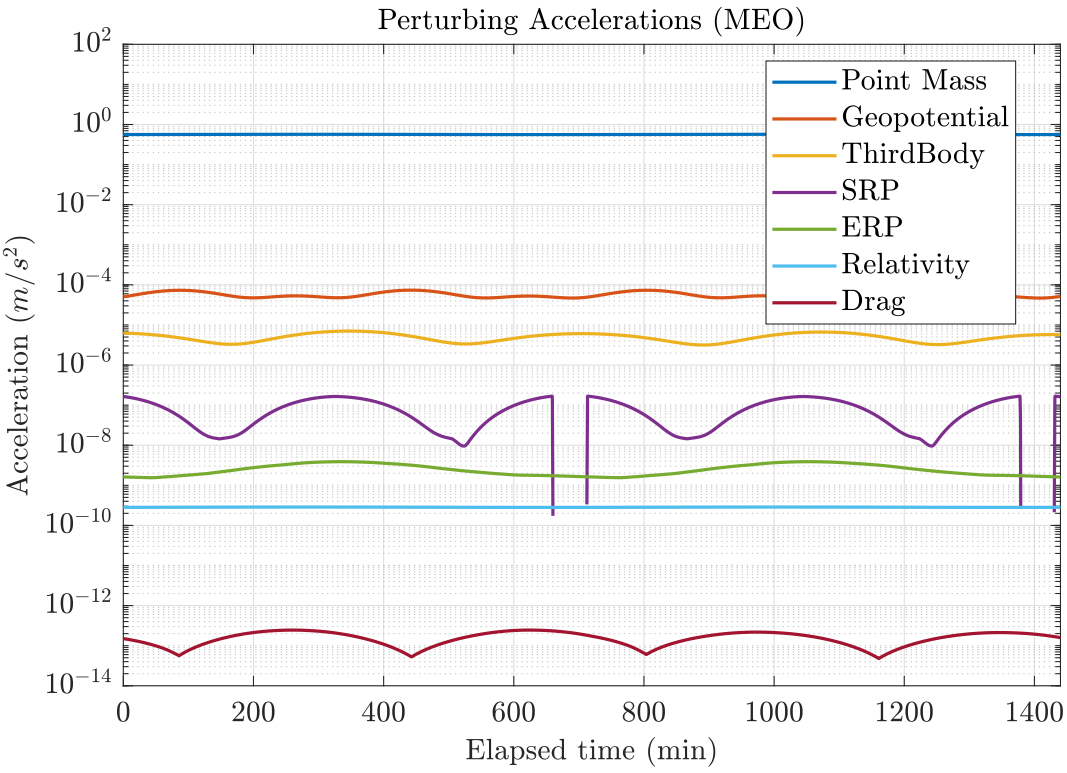

(a) Accelerations

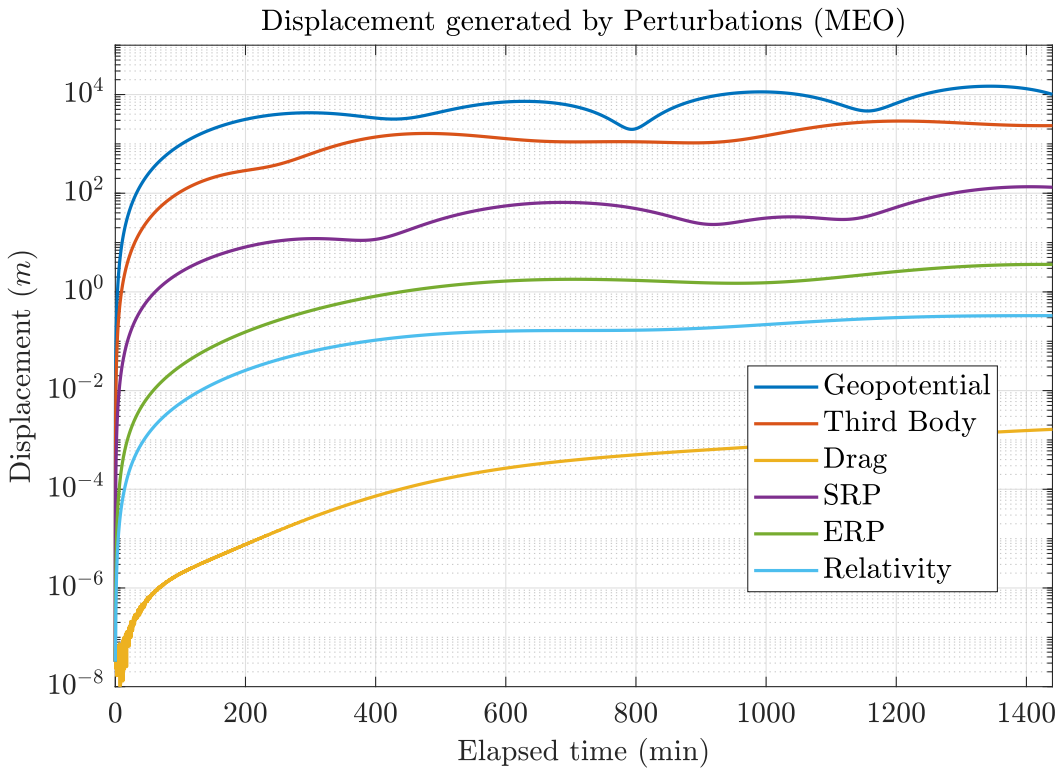

(b) Displacements

Figure 5.4: Perturbation Effects in MEO

The HEO analysis, shown in fig. 5.5, produced quite peculiar patterns. In fact, the acceleration peaks are remarkable for the forces which depend on the altitude. It must be noted that drag is negligible for the majority of the orbit, whereas it becomes the second most important perturbation in proximity of the perigee. Interestingly, SRP and ERP accelerations show that no eclipses occur during the 24 hours of propagation. This is due to the particular orbit configuration.

By looking at the displacements, the most noticeable feature is the drastic deviation caused by aerodynamic drag due to the perigee passage. Again, even though the acceleration only show brief peaks, the deviation caused by this sudden increase is kept also after the perigee, making drag the most important non conservative force also in this particular case.

Finally, the Geostationary case is reported in fig. 5.6. Here the Geopotential and Third Body accelerations are practically equal. SRP acceleration has notably increased, becoming the dominant non conservative force. Drag is completely negligible, as the atmosphere is completely absent at the Geostationary altitude. Apart from that, no other remarkable features are visible, due also to the absence of eclipses. These descriptions remain valid also in the case of the displacement analysis.

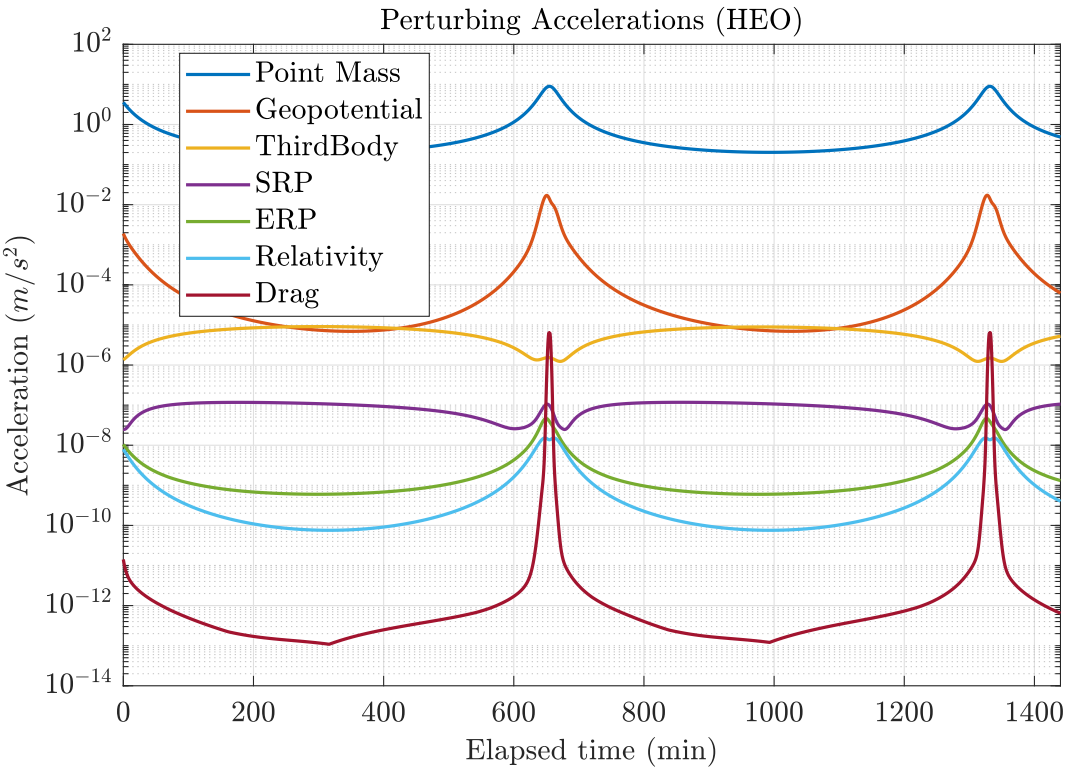

(a) Accelerations

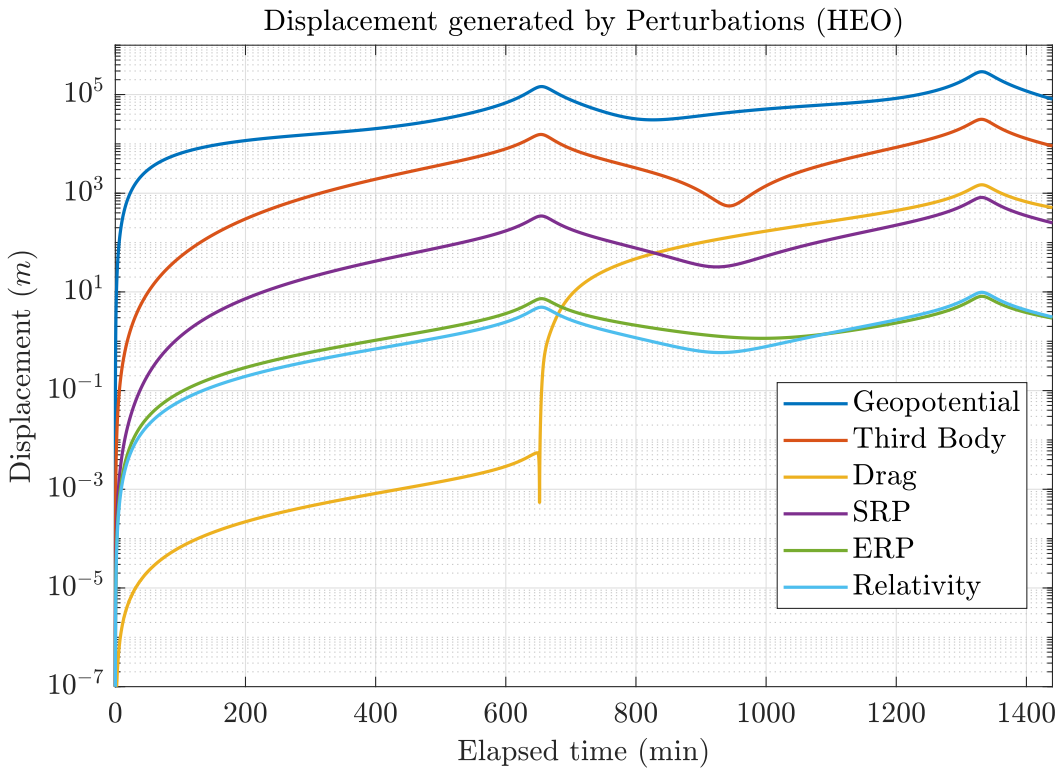

(b) Displacements

Figure 5.5: Perturbation Effects in HEO

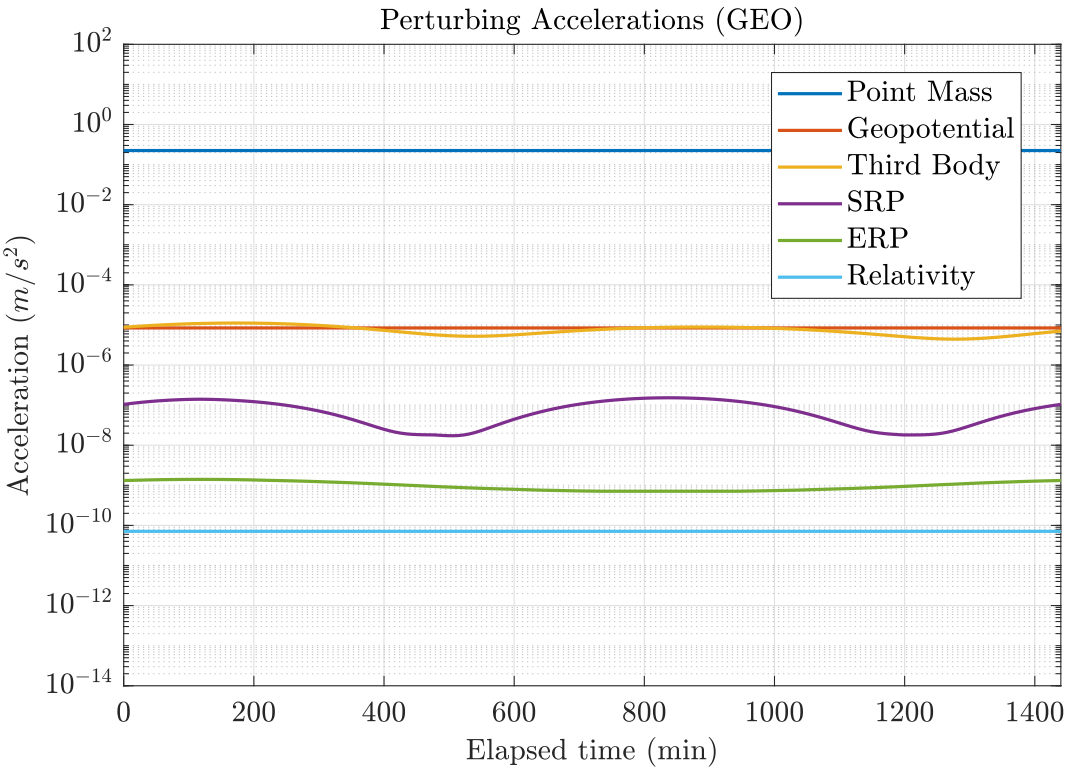

(a) Accelerations

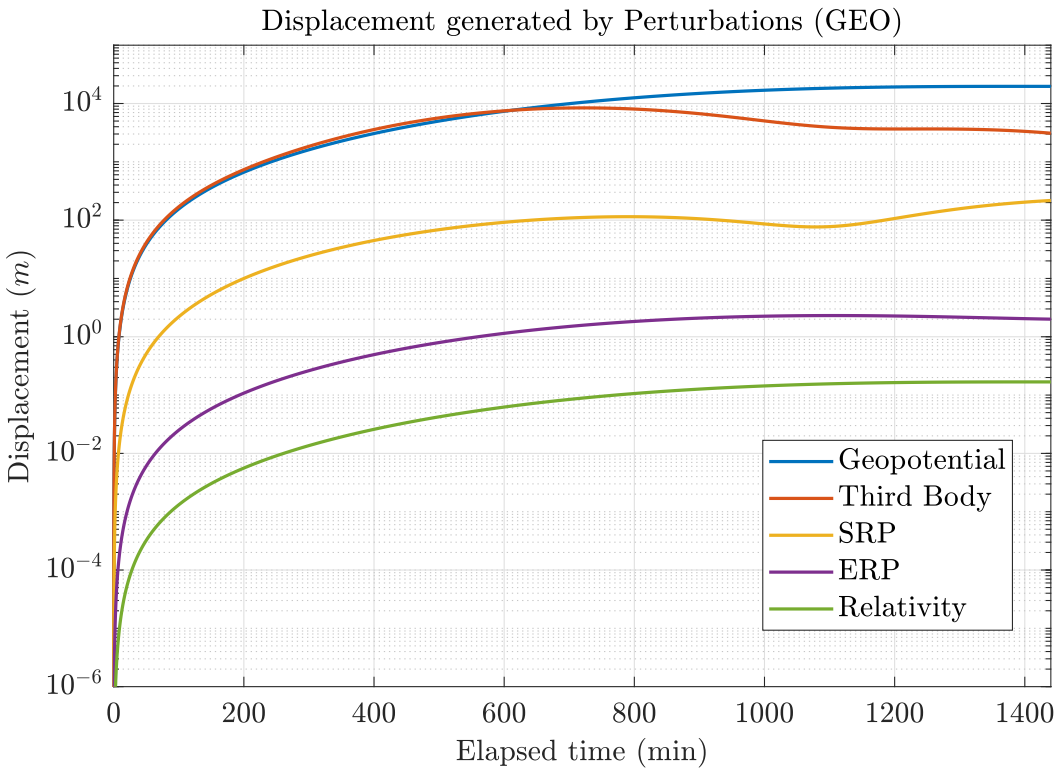

(b) Displacements

Figure 5.6: Perturbation Effects in GEO

5.2. Model Sensitivity Analysis

From the discussion in chapter 3 it was clear that, when considering advanced dynamical models, multiple choices within the same perturbation formulation can be adopted. As these choices can potentially result in significant effect variation, a sensitivity analysis regarding some of the implemented perturbations was conducted.

5.2.1. Geopotential Model Choice

As shown previously, the effect of the Earth's oblateness, which causes a deviation from the nominal spherical gravity field, is the perturbation which causes the largest position deviations for all the orbital regimes considered. It is also important to remember that the gravity field formulation depends exclusively on the chosen model, which determines not only the spherical harmonics coefficients, but also the values of the gravity constant and radius of the planet. For this reason, it is useful to understand to what extent a choice of different geopotential models can impact the propagation.

In chapter 3 the advent of Time Varying Geopotentials was described, therefore to run this analysis a TVG model, the GOCO06s, was used. The results obtained with this model were then compared to the ones resulting from a propagation with the classic EGM2008 model. Both the gravity fields were truncated at degree and order 200. The evolution of the position difference between the two results is depicted in fig. 5.7. To resemble a worst-case analysis LEO regime was chosen, as this perturbation is greatest in low altitude orbits.

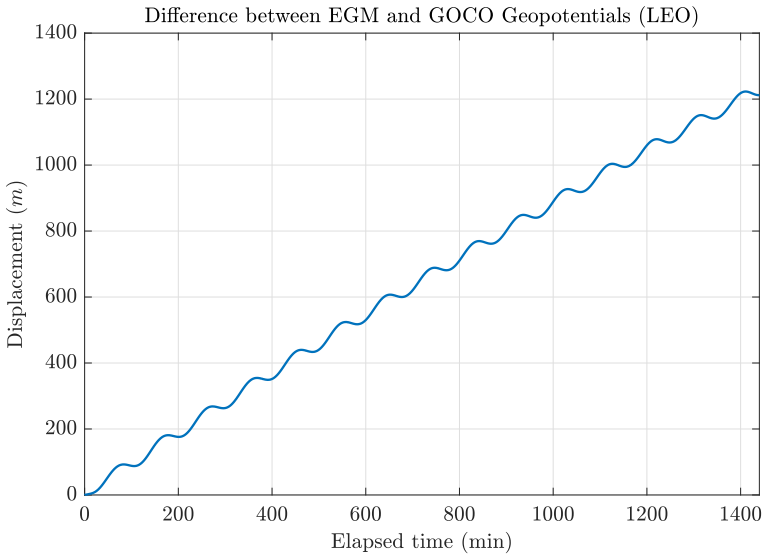

Figure 5.7: Position Difference with different Geopotential Models

The deviation surpasses the value of one kilometer after 24 hours of propagation. This result is extremely valuable as it highlights that simply using different models (i.e. different spherical harmonics coefficients) can lead to deviations which are greater than the ones computed in past analyses concerning the gravity field truncation degree [34]. As such, extreme care needs to be taken when considering the adoption of a particular gravity field formulation. It is expected that more recent models, which can exploit more precise measurements coming from the latest geodesy missions, perform better in terms of accuracy in the gravity field reconstruction. However, this needs to be addressed in future work, possibly involving also the figures of merit for the uncertainty of the coefficients.

Finally, although not reported in plots here, the difference between the effects of using the full Time Varying formulation of the GOCO model and the one instead using only the static part of the field of the same model, was computed. For the considered epoch, the deviation between the two cases reached values in the orders of tenth of centimeters. This highlights that the time varying part of the field contributes to an almost negligible extent, or at least in much lesser part than the choice of the model itself, and can only become relevant for higher propagation times.

5.2.2. Density Model Choice

One of the fundamental parameters for the modelling of the aerodynamic drag is the atmospheric density. Often, this is also the contribution with the highest uncertainties. As seen in chapter 3, lots of models have been developed through the decades, therefore the impact of this choice needed to be investigated.

Trivially, also for this analysis the propagation was carried out in LEO, as for sure it is the class of orbits which experience drag the most. The analysis saw the use of four different density models: the classic US Standard Atmosphere, the established models, prescribed by the ECSS, NRLMSIS-00 and JB2008, and one of the most recent ones, DTM2020. The deviation from a nominal Kepler orbit, caused by aerodynamic drag employing the four models cited above, is reported in fig. 5.8.

The main takeaway from the results of this analysis is the confirmed high variability in the propagation results induced by this parameter. In fact, between the model corresponding to the highest displacement (NRLMSIS-00) and the one with the lowest (US Standard Atmosphere), there is an effect difference of more than 50%. In addition, as the analysed epoch of propagation was characterised by medium level solar activity, these differences are expected to grow in timespans closer to the maximum of the solar activity cycle. The shown variability needs to be considered when choosing a particular density model.

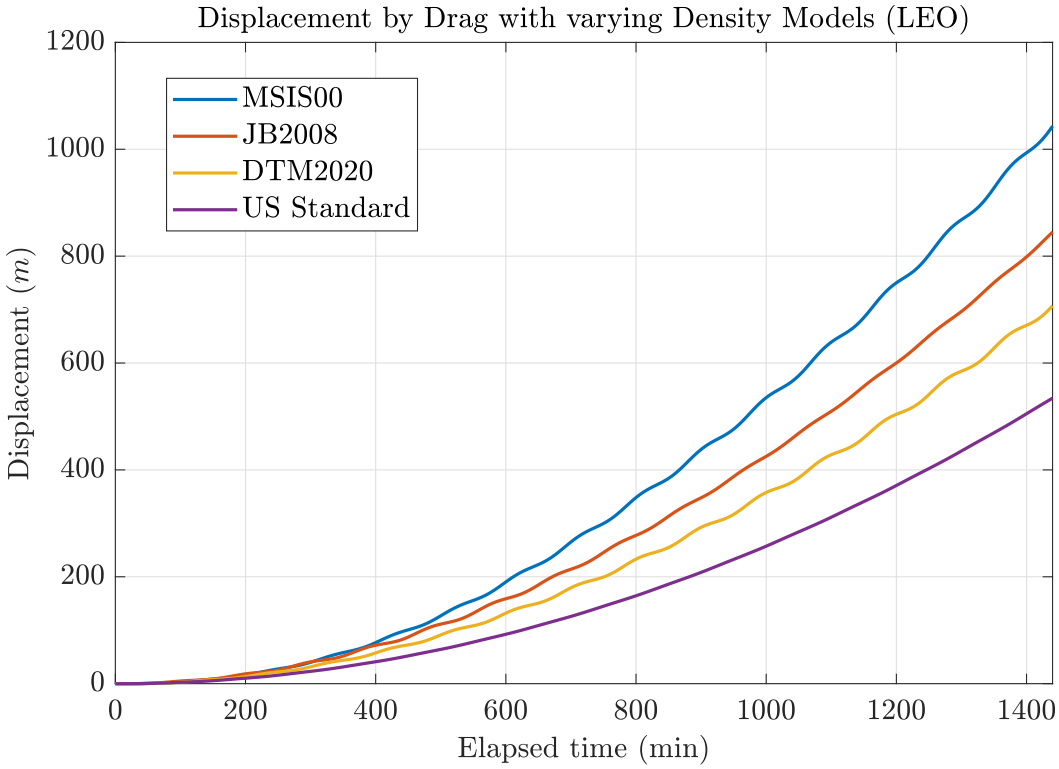

Figure 5.8: Position Difference with different Density Models

A final remark is done about the DTM2020 model. Its displacement highlights an average density value which is significantly lower than the other empirical atmospheric models. This confirms the statements of the developers of the models themselves [4].

5.2.3. Planetary Effects

In the previous section it was very clear how the third body perturbation, as the gravity effects in general, can be one of the most important effects on the satellite orbit. In fact, for high altitude satellites the magnitude of the displacement caused by this force can even be equal to the one due to the geopotential of the Earth.

However, this dynamical model greatly depends on the celestial bodies the gravitational effects of which are considered. Nevertheless, it is not trivial to understand the contributions which can be safely neglected and which one to consider instead. For this reason, an analysis on the effect of every relevant celestial body of the Solar System was carried out for the Geostationary orbit case, which is mostly interested by this perturbation. In particular, every planet of the system was considered, jointly with the perturbations coming from the Sun and the Moon. The displacements caused by these bodies is shown in fig. 5.9.

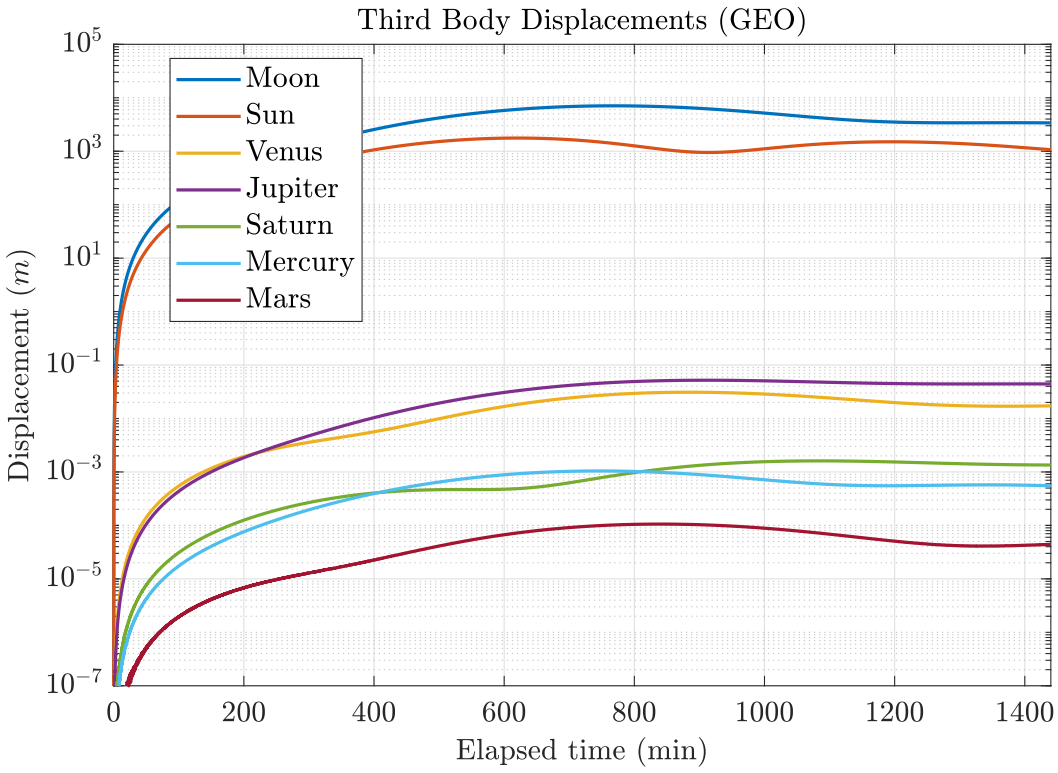

Figure 5.9: Third Body Displacement by Solar System Bodies

As can be seen from the plot, the Moon and the Sun have certainly the greatest effect, causing displacements of more than one kilometer. For what concerns the planetary displacements, the most important ones are from Jupiter and Venus, causing cm-level deviations. Saturn and Mercury follow up, with mm-level displacements. Mars third body effect is smaller. The remaining planets of the outer Solar System were not reported as their magnitudes were even lower. It appears clear that apart from the Moon and Sun, inclusion of the effects by Venus and Jupiter, as also stated in the ECSS [1], should be enough for most applications. An interesting remark is done about Mercury. In fact, one would expect it to have significantly lower effects with respect to Mars. However, as the third body effect greatly depends also on the distance, these perturbations depend on the Solar System "configuration" at the interested epoch. In fact, by looking at where the planets of the inner Solar System were located at the start epoch, represented in fig. 5.10, it is clear how in that time of the year the Earth-Mercury distance was significantly lower than the Earth-Mars distance, hence causing a larger effect. An extended an thorough analysis of this force would need to consider effects averaged over a longer timespan to be completely accurate, but this was out of the scope of this Thesis.

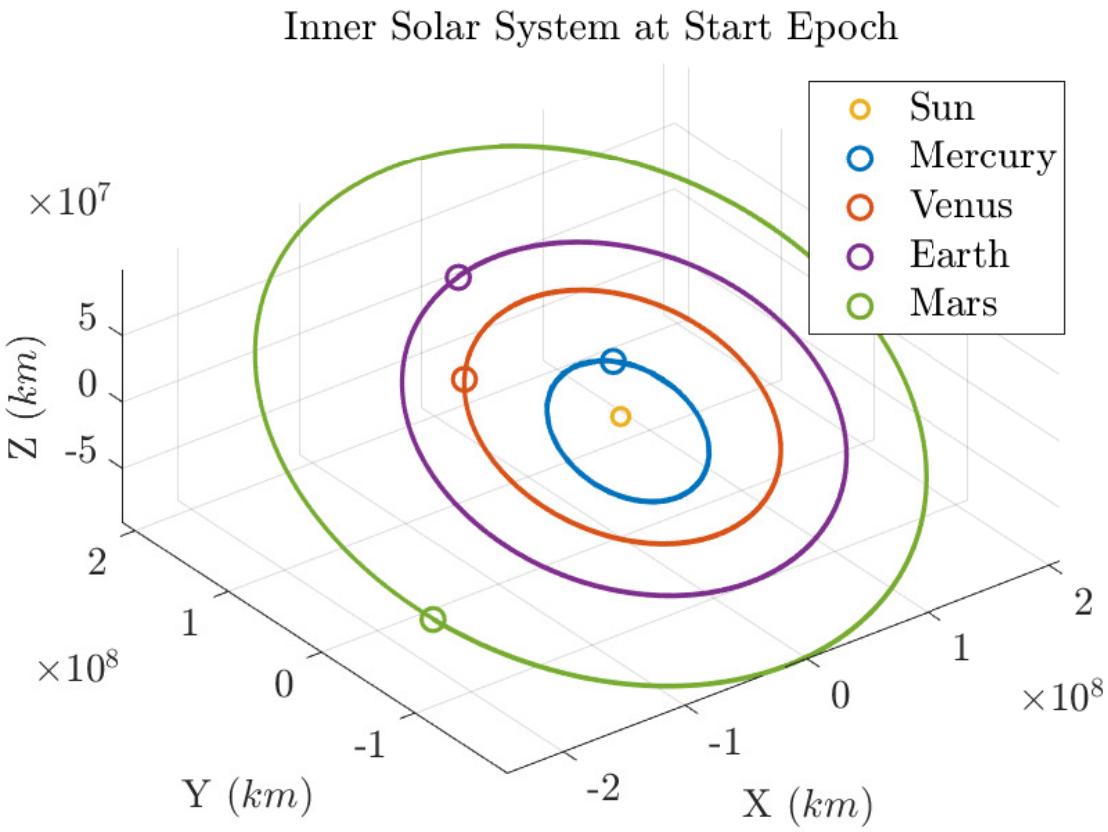

Figure 5.10: Planetary Locations at Start Epoch

5.2.4. Shadow Model Choice

As reported in chapter 3, another particular choice that can be made inside the Propagator is the one of the shadow model for Earth eclipses. This impacts both SRP and ERP. In this regard, the two alternatives which can be selected are a purely geomtetrical dual cone model, and a more "physical" formulation which takes into account all the atmosphere phenomena which can alter the quantity of sunlight which reaches the spacecraft. One could trivially expect the more sophisticated model to provide more realistic and meaningful behaviours, nevertheless it is useful to understand to what extent do the two results differ.

For this analysis, the shadow factor obtained with the two shadow models was investigated for the LEO case. The shown results were restricted to an analysis of the shadow factor for a small timespan coincident with the entering of eclipse of the spacecraft, as the behaviour is almost symmetrical with respect to the case of exiting eclipse. The two shadow factors behaviours are shown in fig. 5.11.

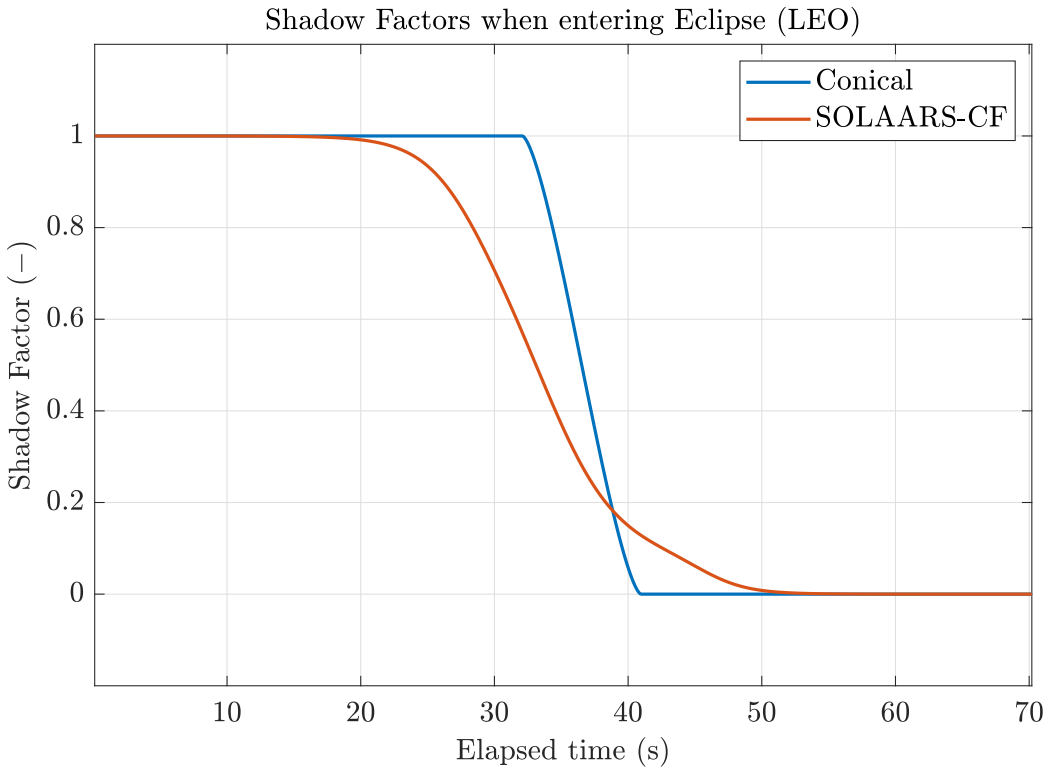

Figure 5.11: Shadow Factors entering Eclipse

Interestingly, the penumbra period computed with the classical model lasts about 8 seconds, whereas the one obtained with the more refined formulation, lasts for around 30 seconds. This means that we obtained an increase of penumbra time by almost a factor 4, in accordance with previous findings in similar LEO scenarios [35]. This result may be useful for two different aspects: first of all, there is a mismodelling of the acceleration of SRP and ERP, as the calculation of the shadow factor is a primary issue in these formulations. Secondly, as the spacecraft power mainly comes from the solar panels, modelling of the quantity of sunlight reaching the satellite is fundamental for accurate sizing of such subsystem. Considering that, as saw previously, a LEO satellite depending on orbit geometry can experience a high number of eclipses even in just 24 hours, accumulating the mismodelled penumbra time over the whole mission duration could lead to the discovery of non-negligible systematic errors.

5.3. Computational Effort Analysis

Even though accuracy is the main requirement of the developed Propagator, it is still important to maintain the computational time required by the propagation under a rea-

sonable limit. However, most of it depends on the propagation configuration selected via the input file. In fact, the computational cost will depend on a variety of factors chosen by the users, as the choice of the numerical integrator, the selected stepsize and the dynamical models to include in the propagation. As past works already analysed the impact of the integrators and stepsize on the duration of the program execution [31], the new analyses focused instead on how the different forces alter the speed of the software.

Therefore, a computational effort analysis was carried out by calling for a relatively high number of times (in the order of thousands calls) the acceleration computation for each force model, using a randomized input state. Consequently, the average time for each force model call was computed. Finally, as the geopotential, calculated up to degree and order 70, showed to be the heaviest force model in terms of numerical cost by some orders of magnitude, the other perturbation contribution were scaled by the average computational cost of such model, equal to 9 ms per call. The scaled results are represented in fig. 5.12.

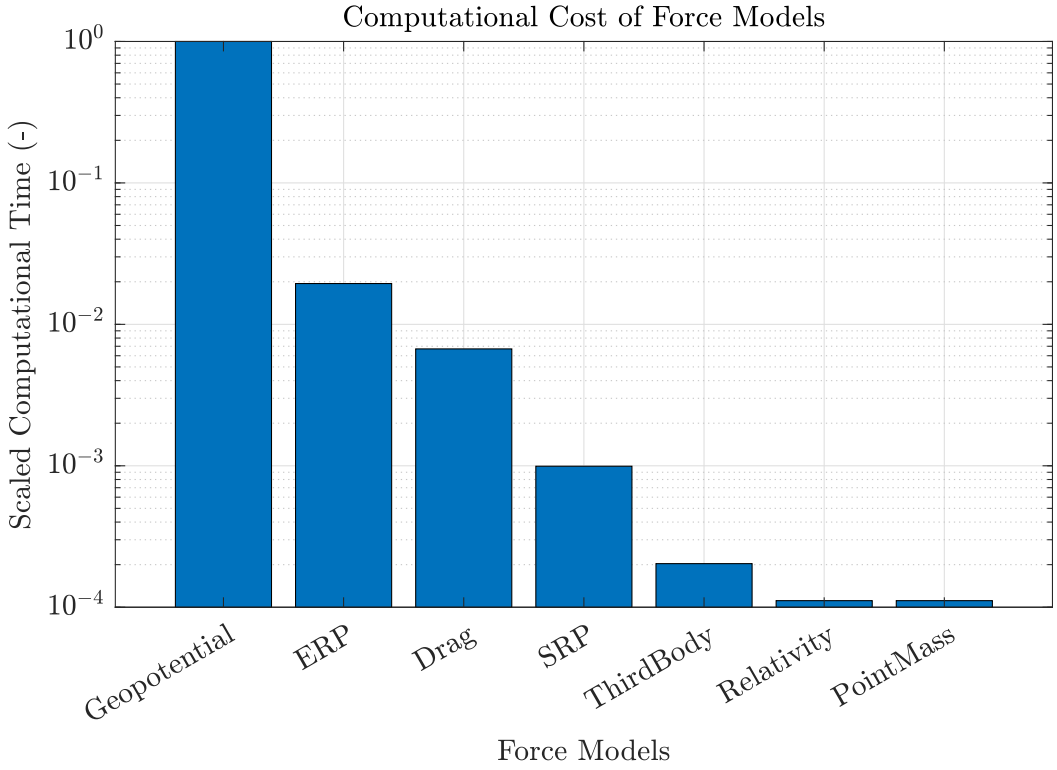

Figure 5.12: Force Models Scaled Computational Cost

As said, the geopotential was the heaviest force, for a variety of reasons. First of all, due to the spherical harmonics formulation, depending on the truncation degree many operations have to be carried out at each call. Furthermore, due to the way this perturbation is

formulated, the acceleration in the Earth-fixed frame is provided, thus requiring a frame conversion, which is also computationally expensive.

The non-conservative forces were the second heaviest dynamical models. ERP and Drag exhibited average times of about 1% of the geopotential, while the SRP closer to 0.1% of such model. These behaviours can be explained by their more complex formulation. In fact, ERP has to calculate the incoming rays from 19 discretized surface elements, whereas drag relies on external models for the computation of parameters like the atmospheric density. In addition, all of them have to deal with the modelling of the satellite surfaces, which is also computationally expensive.

Finally, the remaining gravity-related forces were definitely faster to compute thanks to their relatively simple and compact analytical formulations, with no particular parameters to calculate.

5.4. Discontinuity Control Analysis

An additional study was set up to investigate the effect of the implementation of the discontinuity control in the numerical integrators. In fact, for the reasons listed in chapter 4, the error obtained when trying to reconstruct the total ΔV caused by an Orbital Control Maneuver is expected to be mitigated.

To investigate this issue, the following test case was set up: a "dummy" propagation was set, in the sense that the only force model included was the thrust generated by an input maneuver. As this would be the only acceleration contribution, by comparing the final and initial velocities, we can obtain an estimate of the total ΔV generated by such maneuver. The nominal ΔV is known a-priori thanks to the analytical formulation which relates it to the thrust, reported in eq. (3.45). Therefore, an error can be computed by comparing the nominal ΔV coming from eq. (3.45) with the one obtained by comparing initial and final state of the propagation. This was done with varying input ΔV values, and including and excluding the discontinuity control previously described. The result of this is reported in fig. 5.13.

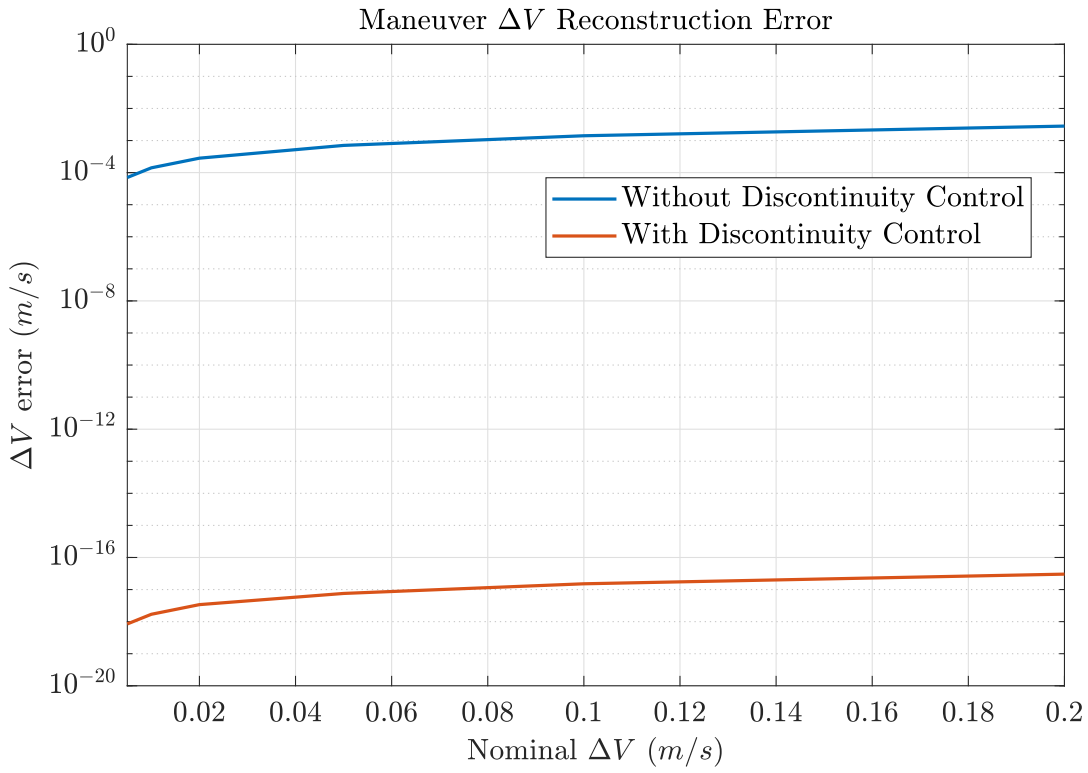

Figure 5.13: Discontinuity Control Effect

Clearly, the implementation of this feature drastically decreased the error due to maneuvers, which now is practically zero. This proves not only the effectiveness of the implemented solutions, but also the presence of the mentioned issues, which could have jeopardized the accuracy in case of maneuvers. Interestingly, the ΔV error, both with and without the discontinuity control, is seen to linearly increase with the nominal ΔV of the maneuver.

5.5. Propagator Validation

Even though any newly introduced Propagator component was thoroughly tested before acceptance, it is still necessary to validate the overall propagation results. This was done following the same philosophy of past propagation software validations [24, 26, 34]. As such, the STK program was chosen as reference solution for the validation simulations.

This process was carried out by propagating the initial state with only the central body acting plus an additional perturbation. The forces considered, apart from the central gravity itself, were the geopotential, the third body perturbation, the SRP and aerodynamic drag. These solutions were then compared to the ones obtained via STK using the

most similar input configurations as possible. It is important to state that this method does not allow to identify the "best" solution between the two, due to the fact that a great amount of uncertainty parameters are present, from the used values of physical constants to the way the softwares are programmed.

The difference between the results obtained with the two softwares is shown in fig. 5.14.

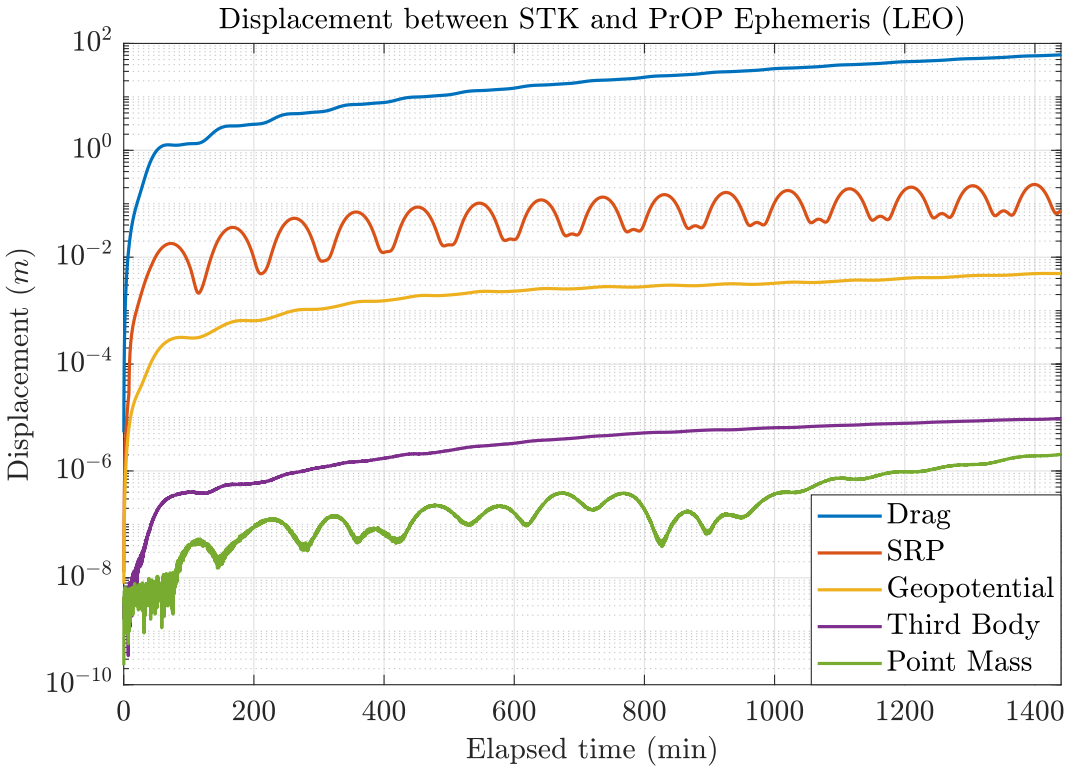

Figure 5.14: Comparison of Propagation Results

First of all, it is clear that modelling of gravitational forces is well in accordance between the two softwares. In fact, at most mm-level differences are reached after 24 hours of progation when using the geopotential perturbation, in this case using the EGM2008 model truncated at degree and order 100 (the maximum degree available in STK). In addition, also SRP modelling quite agrees with the formulation of PrOP. In fact, only cm-like deviations are reached at the end of the integration. These can be attributed to very small differences in the way the solar flux constant is calculated in time. The only perturbation which shows non-negligible differences is the drag. However, this is in accordance with past comparison analyses [34]. The main uncertainty in the modelling of aerodynamic drag, as already stated in chapter 3, is in the calculation of atmospheric density, in this case computed through the US Standard model. In fact, the complex and often "external" modules for the computation of this parameter greatly vary in their practical implemen-

tations and formulations. Other sources of uncertainties in the case of empirical models is the way space weather data is treated. In fact, the choice of interpolation method, as choosing if using daily or hourly data, can induce results differences in the order of magnitude of choosing a completely different empirical models [34]. As such, the obtained result is still considered acceptable.

All the final deviation values were in agreement with the threshold values used in past validation analyses, therefore the comparison was considered successful.

6 | Conclusions and Future Developments

The objective of this Master Thesis was to continue the development of the Precise Orbit Propagator, focusing on the improvement of already present dynamical models and on the inclusion of previously neglected perturbations. In particular, the Earth Radiation Pressure and Relativity perturbations were implemented from scratch, while the Geopotential, Aerodynamic Drag and Solar Radiation Pressure experienced an expansion in terms of available models and parameter computation.

For what concerns the numerical integration segment of the software, a new discontinuity control technique was employed in the integrators to deal with the errors introduced by the presence of orbital control maneuvers during the propagation.

Following these implementations, several assessment studies were carried out to analyse the impact of the components of the Dynamics library of the software on the propagation results. First of all, the accelerations and displacements caused by each single perturbation on a set of four Kepler orbits, chosen in a way as to represent the main Earth-orbiting regimes, were computed. The results confirmed most of the already known acceleration hierarchies varying with altitude, but were useful to gather the orders of magnitudes of such effects. The Geopotential perturbation confirmed to be the major acceleration for Earth-orbiting satellites after the central gravity effect, even though experiencing a decrease in magnitude with increasing altitude. Third Body effects coming from the Sun and the Moon, on the contrary, increased with altitude, and were higher than any higher non-conservative forces, except for the LEO case. Aerodynamic Drag was the second most important perturbation for the LEO scenario, but was negligible for the higher altitude orbits, except for the HEO were the low altitude of the perigee made Drag effects quite visible. SRP confirmed to be the most important non-conservative force for high altitude spacecrafts. Finally, ERP and Relativity effects were sensibly smaller than the other forces, both showing diminishing magnitudes for higher orbital regimes.

In addition, a sensitivity analysis was carried out to investigate the variation of pertur-

bation effects with varying environmental and dynamical configurations. The choice of the Geopotential model proved to be very significant, causing quite different displacement depending on the coefficients used. Similarly, Aerodynamic Drag effects reported great variability depending on the model used for the calculation of the atmospheric density. An analysis on the Third Body effects coming from the main celestial bodies of the Solar System showed that, apart from the accelerations caused by the Sun and the Moon, the major planetary perturbations are due to Venus and Jupiter. Furthermore, the study regarding the shadow model employed for the calculation of the occultation caused by the Earth, highlighted a difference by a factor four between a dual-cone and the SOLAARS realistic model. Finally, a computational effort analysis showed that the Geopotential is the heaviest effect to calculate, followed by all the non-conservative forces. The acceleration due to the central gravity, third bodies and relativity required negligible amounts of time.

The study of the ΔV reconstruction error in the presence of control maneuvers showed how the implementation of the discontinuity control process allowed to minimize the issues cause by discontinuous accelerations.

Finally, the propagation results were compared to the ones obtained with the well-established commercial flight dynamics software STK, for the main perturbations. The comparison allowed to successfully validate the developed Propagator.

For what concerns possible future developments of the software, possible extensions can be made on the formulation of the satellite coefficients for Aerodynamic Drag and Radiation Pressure. In fact, as of now only constant parameters are implemented, nevertheless more complex formulations based on fluid dynamics and optics can be explored. In addition, the ERP modelling could be improved by increasing the number of discretized surface elements and computing the Earth radiation on the basis of outsourced space weather data. In addition, discontinuities introduced by eclipses should be taken into account. Due to the fact that the exact eclipse discontinuity moment, differently from control maneuvers, is not known a-priori, it is possible that the discontinuity control process shall be modified to achieve this further result.

A further analysis step is certainly the one concerning the validation of the propagation results against real satellite ephemeris. This aspect would be complex due to the number of variables which affect real satellite motion and can be modelled only up to a certain extent. Nevertheless, a successful validation of this kind would definitely open up the Precise Orbit Propagator to its intended original use.

Bibliography

[1] European cooperation for space standardization (ecss) website - active standards. https://ecss.nl/standards/active-standards/. Accessed: 2022-11-18.

[2] Ansys stk product page. https://www.ansys.com/products/missions/ansys-stk. Accessed: 2022-10-30.

[3] B. Bowman, W. K. Tobiska, F. Marcos, C. Huang, C. Lin, and W. Burke. A new empirical thermospheric density model jb2008 using new solar and geomagnetic indices. In *AIAA/AAS Astrodynamics Specialist Conference and Exhibit*, 2008. doi: 10.2514/6.2008-6438.

[4] Bruinsma, Sean and Boniface, Claude. The operational and research dtm-2020 thermosphere models. *J. Space Weather Space Clim.*, 11:47, 2021. doi: 10.1051/swsc/2021032. URL https://doi.org/10.1051/swsc/2021032.

[5] D. P. Drob, J. T. Emmert, J. W. Meriwether, J. J. Makela, E. Doornbos, M. Conde, G. Hernandez, J. Noto, K. A. Zawdie, S. E. McDonald, J. D. Huba, and J. H. Klenzing. An update to the horizontal wind model (hwm): The quiet time thermosphere. *Earth and Space Science*, 2(7):301–319, 2015. doi: https://doi.org/10.1002/2014EA000089. URL https://agupubs.onlinelibrary.wiley.com/doi/abs/10.1002/2014EA000089.

[6] W. M. Folkner, J. G. Williams, D. H. Boggs, R. S. Park, and P. Kuchynka. The Planetary and Lunar Ephemerides DE430 and DE431. *Interplanetary Network Progress Report*, 42-196:1–81, Feb. 2014.

[7] K. Gutsche, T. Hobiger, S. Winkler, and B. Stucke. Podcast: Precise orbit determination software for leo satellites. In *Proceedings of the 35th International Technical Meeting of the Satellite Division of the Institute of Navigation (ION GNSS+ 2022)*, 2022.

[8] S. Hackel. *Refinement of Reduced-Dynamic Orbit Determination for Low Earth Satellites*. PhD thesis, Technische Universität München, 2019.

[9] C. Huang, J. C. Ries, B. D. Tapley, and M. M. Watkins. Relativistic Effects for Near Earth Satellite Orbit Determination. *Celestial Mechanics and Dynamical Astronomy*, 48(2):167–185, June 1990. doi: 10.1007/BF00049512.

[10] S. Hughes, R. Qureshi, S. Cooley, and J. Parker. Verification and validation of the general mission analysis tool (gmat). In *AIAA/AAS Astrodynamics Specialist Conference*, 08 2014. ISBN 978-1-62410-308-7. doi: 10.2514/6.2014-4151.

[11] Z. Kang, P. Nagel, and R. Pastor. Precise orbit determination for grace. *Advances in Space Research*, 31:1875–1881, 04 2003. doi: 10.1016/S0273-1177(03)00159-5.

[12] P. Knocke. *Earth Radiation Pressure Effects on Satellites*. PhD thesis, Center for Space Research, University of Texas, Austin, Texas, 1989.

[13] A. Kvas, J. M. Brockmann, S. Krauss, T. Schubert, T. Gruber, U. Meyer, T. Mayer-Gürr, W.-D. Schuh, A. Jäggi, and R. Pail. Goco06s – a satellite-only global gravity field model. *Earth System Science Data*, 13(1):99–118, 2021. doi: 10.5194/essd-13-99-2021. URL `https://essd.copernicus.org/articles/13/99/2021/`.

[14] F. W. Landerer, F. M. Flechtner, H. Save, F. H. Webb, T. Bandikova, W. I. Bertiger, S. V. Bettadpur, S. H. Byun, C. Dahle, H. Dobslaw, E. Fahnestock, N. Harvey, Z. Kang, G. L. H. Kruizinga, B. D. Loomis, C. McCullough, M. Murböck, P. Nagel, M. Paik, N. Pie, S. Poole, D. Strekalov, M. E. Tamisiea, F. Wang, M. M. Watkins, H.-Y. Wen, D. N. Wiese, and D.-N. Yuan. Extending the global mass change data record: Grace follow-on instrument and science data performance. *Geophysical Research Letters*, 47(12):e2020GL088306, 2020. doi: https://doi.org/10.1029/2020GL088306.

[15] C.-D. Munz and T. Westermann. *Numerische Behandlung gewöhnlicherund partieller Differenzialgleichungen*. Springer, 2006.

[16] Y. Nie, Y. Shen, Q. Chen, and Y. Xiao. Hybrid-precision arithmetic for numerical orbit integration towards future satellite gravimetry missions. *Advances in Space Research*, 66(3):671–688, 2020. ISSN 0273-1177. doi: https://doi.org/10.1016/j.asr.2020.04.042. URL `https://www.sciencedirect.com/science/article/pii/S0273117720302945`.

[17] E. G. Oliver Montenbruck. *Satellite Orbits: Models, Methods and Applications*. Springer Berlin, 2000.

[18] U. S. C. on Extension to the Standard Atmosphere. *U.S. Standard Atmosphere, 1976*. NOAA - SIT 76-1562. National Oceanic and Amospheric [sic] Administration, 1976. URL `https://books.google.it/books?id=x488AAAAIAAJ`.

[19] N. K. Pavlis, S. A. Holmes, S. C. Kenyon, and J. K. Factor. The development and evaluation of the earth gravitational model 2008 (egm2008). *Journal of Geophysical Research: Solid Earth*, 117(B4), 2012. doi: https://doi.org/10.1029/2011JB008916.

[20] H. Peter, A. Jäggi, G. Beutler, and U. Meyer. Goce: precise orbit determination for the entire mission. *Journal of Geodesy*, 88, 11 2014. doi: 10.1007/s00190-014-0742-8.

[21] H. Peter, U. Meyer, M. Lasser, and A. Jäggi. Cost-g gravity field models for precise orbit determination of low earth orbiting satellites. *Advances in Space Research*, 69 (12):4155–4168, 2022. ISSN 0273-1177. doi: https://doi.org/10.1016/j.asr.2022.04.005.

[22] G. Petit and B. Luzum. Iers conventions (2010). *Tech. Rep. DTIC Document*, 36: 180, 01 2010.

[23] J. M. Picone, A. E. Hedin, D. P. Drob, and A. C. Aikin. Nrlmsise-00 empirical model of the atmosphere: Statistical comparisons and scientific issues. *Journal of Geophysical Research: Space Physics*, 107(A12):SIA 15–1–SIA 15–16, 2002. doi: https://doi.org/10.1029/2002JA009430. URL `https://agupubs.onlinelibrary.wiley.com/doi/abs/10.1029/2002JA009430`.

[24] M. Poderico and G. Morani. Validation of tools for 3dof orbital dynamics simulation. *American Journal of Engineering and Applied Sciences*, 13:649–657, 04 2020. doi: 10.3844/ajeassp.2020.649.657.

[25] R. Robertson. *Highly Physical Solar Radiation Pressure Modeling During Penumbra Transitions*. PhD thesis, Department of Aerospace and Ocean Engineering at Virginia Polytechnic Institute and State University, Blacksburg, Virginia, 04 2015.

[26] C. Robson. The design and validation of a spacecraft orbit and attitude simulation environment in matlab/simulink. Master's thesis, University of Alberta, 09 2018.

[27] K.-m. Roh, S. Kopeikin, and J.-H. Cho. Numerical simulation of the post-newtonian equations of motion for the near earth satellite with an application to the lares satellite. *Advances in Space Research*, 58, 08 2016. doi: 10.1016/j.asr.2016.08.009.

[28] S. Rudenko, D. Dettmering, S. Esselborn, T. Schöne, C. Förste, J.-M. Lemoine, M. Ablain, D. Alexandre, and K.-H. Neumayer. Influence of time variable geopotential models on precise orbits of altimetry satellites, global and regional mean sea level trends. *Advances in Space Research*, 54(1):92–118, 2014. ISSN 0273-1177. doi: https://doi.org/10.1016/j.asr.2014.03.010.

[29] L. H. Sentman. Free molecule flow theory and its application to the determination of

aerodynamic forces. Technical report, Lockheed Missiles and Space Company Inc., 1961.

[30] K. Sośnica, G. Bury, R. Zajdel, K. Kazmierski, J. Ventura-Traveset, R. Prieto-Cerdeira, and L. Mendes. General relativistic effects acting on the orbits of Galileo satellites. *Celestial Mechanics and Dynamical Astronomy*, 133(4):14, Apr. 2021. doi: 10.1007/s10569-021-10014-y.

[31] B. Stucke. Development of a satellite trajectory generator for precise orbit determination. Master's thesis, Institut für Navigation, Universität Stuttgart, 2022.

[32] B. Tapley, B. Schutz, J. Ries, and C. Shum. Precision orbit determination for topex. *Advances in Space Research*, 10(3):239–247, 1990. ISSN 0273-1177. doi: https://doi.org/10.1016/0273-1177(90)90354-3. URL `https://www.sciencedirect.com/science/article/pii/0273117790903543`.

[33] B. Tapley, M. Watkins, F. Flechtner, C. Reigber, S. Bettadpur, M. Rodell, I. Sasgen, J. Famiglietti, F. Landerer, D. Chambers, J. Reager, A. Gardner, H. Save, E. Ivins, S. Swenson, C. Boening, C. Dahle, D. Wiese, H. Dobslaw, and I. Velicogna. Contributions of grace to understanding climate change. *Nature Climate Change*, 5, 04 2019. doi: 10.1038/s41558-019-0456-2.

[34] D. Vallado. An analysis of state vector propagation using differing flight dynamics programs. In *AAS Space Flight Mechanics Conference*, 01 2005.

[35] K. Vielberg and J. Kusche. Extended forward and inverse modeling of radiation pressure accelerations for leo satellites. *Journal of Geodesy*, 94, 04 2020. doi: 10.1007/s00190-020-01368-6.

[36] M. Wermuth, A. Hauschild, O. Montenbruck, and A. Jäggi. Terrasar-x rapid and precise orbit determination. In *21st International Symposium on Space Flight Dynamics*, 01 2009.

[37] S. C. Wu, T. P. Yunck, and C. L. Thornton. Reduced-dynamic technique for precise orbit determination of low earth satellites. *Journal of Guidance, Control, and Dynamics*, 14(1):24–30, 1991. doi: 10.2514/3.20600. URL `https://doi.org/10.2514/3.20600`.

List of Figures

List of Tables